Journal of Volcanology and Geothermal Research 455 (2024) 108205

Contents lists available at ScienceDirect

Journal of Volcanology and Geothermal Research

journal homepage: www.journals.elsevier.com/journal-of-volcanology-and-geothermal-research

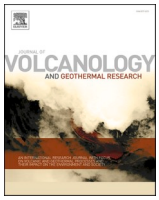

Conditions for formation and preservation of andesite-hosted mafic enclaves during the 2018 Lower East Rift Zone eruption of Kīlauea

Rose Gallo [a,*], Thomas Shea [a], Alan Whittington [b], Ashley Emerson [b], Joseph Boro [c], Adrien J. Mourey [d]

[a] Department of Earth Sciences, University of Hawai'i at Mānoa, 1680 East-West Rd, Honolulu, HI 96822, USA
[b] Department of Earth and Planetary Sciences, The University of Texas at San Antonio, San Antonio, TX 78249, USA
[c] Lawrence Livermore National Laboratory, 7000 East Ave, L-231, Livermore, CA 94551, USA
[d] Earth Observatory of Singapore, Nanyang Technological University, Singapore, Singapore

ARTICLE INFO

Keywords:
Kilauea
Enclaves
Mingling
Andesite
Major element chemistry
Trace element chemistry
Thermal conduction model

ABSTRACT

Andesites erupted at Kīlauea in 2018 in the Lower East Rift Zone for the first time in the known geological record. The evolved lavas erupted at Fissure 17 of the 2018 eruption, ranging from andesites to basaltic andesites, contain abundant mafic enclaves both in the lava flows and the ejecta, which are unusual at Kīlauea and in Hawai'i in general. Textural observations indicate that the enclaves originate from incomplete mixing of two magmas rather than the incorporation of cold basaltic wall rock. We suggest, on the basis of bulk and mineral compositions, that the source of the mafic enclaves is the early 2018 evolved basalt magma (phase 1b) that erupted concomitantly at adjacent fissures, which mixed with the andesite to produce the range of basaltic andesite compositions observed at Fissure 17. The coexistence of homogenized basaltic andesites and mafic enclaves within the same magma require a mixing mechanism resulting in both complete homogenization and preservation of enclaves. We propose that the range of mixing and mingling processes may be explained by spatial and temporal variability in the mixing percentages of the phase 1b basalt and the andesite within the andesite magma chamber. Field observations, chemical compositions, and 2D thermal conduction models suggest that enclaves are preserved where the basalt contribution to mixing is less than roughly 40 %, as a result of microlite crystallization leading to rigidification of the enclave magma. Above this threshold, the mixed magmas became largely homogenized. The scarcity of mafic enclaves at Kīlauea and in the Hawai'i igneous record is likely explained by mixing between magmas that lack sufficient compositional and rheological contrasts to preserve them.

1. Introduction

The 2018 Lower East Rift Zone (LERZ) eruption at Kīlauea was a unique event in its eruptive history, which afforded new insights into the volcano's complex magmatic system (Anderson et al., 2024). This included the first known eruption of andesites at Kīlauea, a volcano well known for its monotonous basaltic eruptions. The eruption highlighted the high degree of hydraulic connectivity between the summit caldera and the LERZ ~40 km away (Patrick et al., 2019) and revealed extremes in mass eruption rate (Dietterich et al., 2021) and composition (Gansecki et al., 2019) not observed before. On May 13th, 2018, ten days after the beginning of the LERZ eruption, andesites and basaltic andesites began to erupt from a 0.5 km-long fissure segment, Fissure 17, offset ~0.25 km north of the other 23 eruptive fissures (Fig. 1). Field observations of the lava flows and ejecta of Fissure 17 revealed the presence of numerous basaltic enclaves within the andesites and basaltic andesites, also reported by Haag et al. (2024) and Soldati et al. (2024). Mafic enclaves have rarely been observed in ocean island volcanoes (Charreteur and Tegner, 2013; Mancini et al., 2015) despite the prevalence of magma mixing processes inferred from geochemistry (Garcia et al., 2000; Helz and Wright, 1992; Ho and Garcia, 1988; Shamberger and Garcia, 2007; Wright, 1971; Wright and Fiske, 1971; Wright and Helz, 1996), presumably because readily miscible basalts dominate in these environments. Kīlauea has erupted basaltic andesites at least once before (Downs et al., 2023; Hazlett et al., 2019), but dominantly produces basalts, and mafic enclaves have never been reported from any

* Corresponding author.
E-mail address: rgallo@hawaii.edu (R. Gallo).

https://doi.org/10.1016/j.jvolgeores.2024.108205
Received 29 May 2024; Received in revised form 3 October 2024; Accepted 4 October 2024
Available online 9 October 2024

previous eruption. The compositional contrast between the enclaves at Fissure 17 and their host lava is smaller than what has generally been documented at other volcanoes (Bacon, 1986; Clynne, 1999; Humphreys et al., 2013; Martin et al., 2006a, 2006b; Mashima, 2004; Plail et al., 2018; Richer et al., 2004).

This paper aims to determine the physical and rheological state of the enclaves at their time of incorporation into the Fissure 17 magmas and to establish their origin. We consider whether the mafic enclaves represent a molten magma that intruded into the Fissure 17 magma body or incompletely digested basaltic wallrock/xenoliths and investigate their potential magmatic sources. Four hypotheses for the source of the enclaves are considered: 1) Active intrusion of the basaltic magma which erupted simultaneously to Fissure 17 from adjacent vents, known as phase 1b, into the andesite body. 2) Incorporation and partial digestion of xenoliths of lava from the early phase of the 1955 eruption, which had two vents (D and M) less than 0.5 km away from Fissure 17 to the north (Figs. 1, 3), Passive intrusion of partially-molten magma stored in the rift zone following the 1955 eruption, as previously proposed by Haag et al. (2024) and Soldati et al. (2024) into the andesite body. 4) Passive intrusion of partially-molten magma stored in the rift zone from an eruption dated to roughly 1790 (Moore and Trusdell, 1991), which had one of its vents approximately 0.7 km from Fissure 17 to the southwest (Fig. 1). Bulk rock and mineral major and trace element compositions, in combination with evidence from the shapes and textures of the mafic enclaves and their contacts with the host lava, argue that the enclaves were derived from the phase 1b lavas of the 2018 LERZ eruption. The phase 1b magma was previously suggested to have mixed with an andesite magma body beneath Fissure 17 to produce the range of andesites to basaltic andesites observed in the eruptive products of Fissure 17 (Gansecki et al., 2019). We then explore the rheological conditions that locally promoted mingling and preservation of enclaves versus mixing and homogenization at different locations along the fissure. This work sheds light on the large-scale dynamics of interaction between the different magmatic end-members involved in the 2018 LERZ eruption. Describing these dynamics is an important component of understanding the processes involved in remobilizing and erupting evolved magmas stored in Kīlauea's rift zones, particularly in this populated portion of the LERZ.

1.1. Background

Mafic enclaves, defined as inclusions of a more mafic rock type within a felsic igneous rock by Wolff (2021), are commonly observed in arc volcanoes around the world (Bacon, 1986; Clynne, 1999; Humphreys et al., 2013; Martin et al., 2006a, 2006b; Mashima, 2004; Plail et al., 2018; Richer et al., 2004). Enclaves are in most cases interpreted to result from mafic magma intruding into a more felsic magma body and mingling to form droplets and globules. The term enclaves has, in some cases, also been used to refer to partially digested xenoliths (Wolff, 2021) or blobs of crystal-mush of a less evolved composition (Winslow et al., 2022), but we will use the narrower and more common definition here (Barbarin and Didier, 1982; Baxter and Feely, 2002; Vernon, 1984). The molten origin of the enclaves considered under this definition is typically inferred from textures such as quenched margins, crenulate margins, overall ellipsoidal shapes of enclaves, visual evidence of mingling at contacts, and exchange of minerals between the host magma and enclaves (Bacon, 1986; Richer et al., 2004; Seaman and Chapman, 2008).

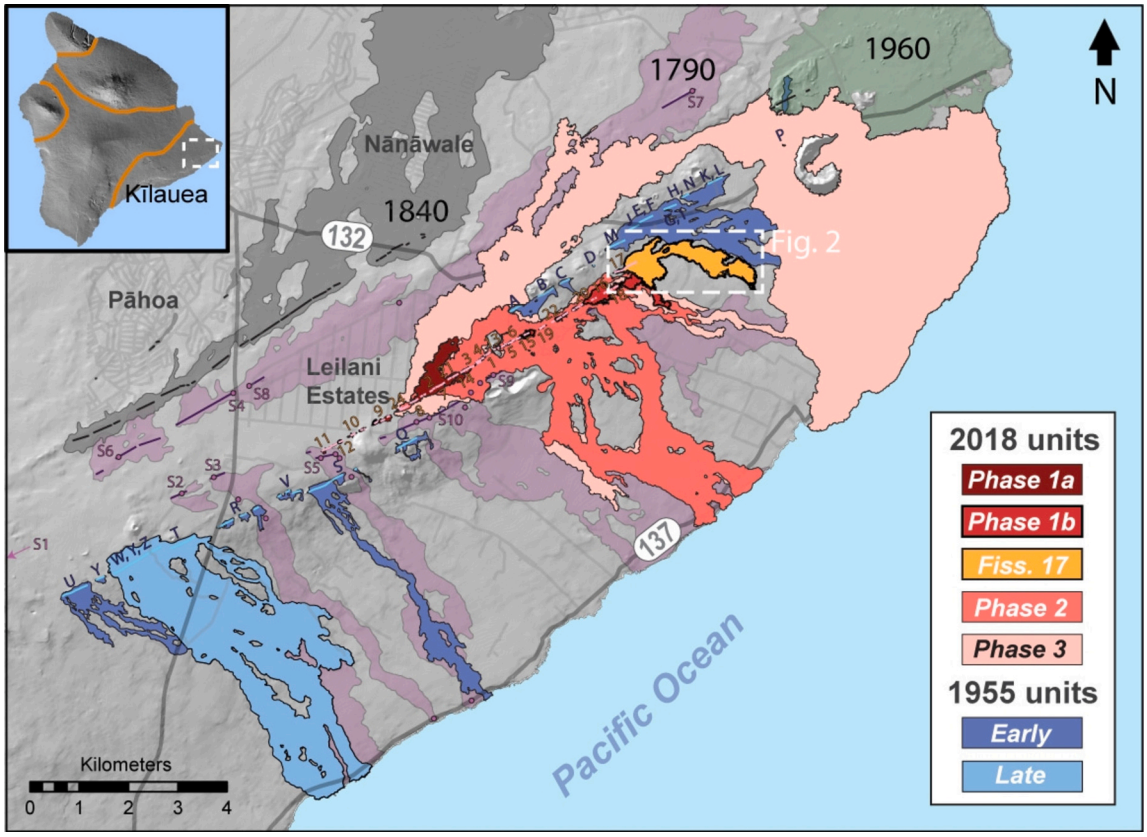

Fig. 1. Map showing the location of the historical lava flows and fissures of the Lower East Rift Zone. The lava flows associated with Fissure 17 are indicated in a white box. Fissure names for the 2018 and 1955 eruptions are shown. Sample sites for the ca. 1790 eruption are indicated with purple points and given one label per fissure. Fissures for other historical eruptions are shown with black lines. Inset shows the location of the Lower East Rift Zone on Kīlauea and the island of Hawai'i with the boundaries of the five subaerial volcanoes delineated. (For interpretation of the references to colour in this figure legend, the reader is referred to the web version of this article.)

When two magmas interact, they may mingle or mix in a variety of ways. We use mingling to refer exclusively to the incomplete physical intermingling of magmas, and mixing to refer to the chemical homogenization of magmas by a combination of physical intermingling and diffusion (Barbarin and Didier, 1982; Charreteur and Tegner, 2013; Sparks and Marshall, 1986). The ability to preserve isolated masses of more mafic magma within a more felsic magma, instead of the formation of banded textures or complete homogenization, requires that the enclave magma become too rigid to mix further on the timescale of the magma interaction either by quenching to glass upon contact or crystallizing to the point of rheological locking. Whether this occurs is dependent on the compositions, initial temperatures, and crystal contents of both magmas, how vigorously they interact, the time period over which they are in contact, and the relative proportions of the two magmas (Andrews and Manga, 2014; Charreteur and Tegner, 2013; Sparks and Marshall, 1986). Various degrees of homogenization between the host magma and the enclave-forming magma may occur simultaneously to the preservation of enclaves as a result of spatially variable mingling and mixing processes within the magma chamber (Bresler et al., 1997; Charreteur and Tegner, 2013; Clynne, 1999; Humphreys et al., 2013; Mashima, 2004; Petrelli et al., 2006; Richer et al., 2004; Ruprecht et al., 2020; Seaman and Chapman, 2008). The occurrence of spatially variable mixing processes has been suggested to be the result of differing proportions of mafic and felsic magma locally present throughout the system (Charreteur and Tegner, 2013; Sparks and Marshall, 1986) or variable local flow behavior within the magma chamber (Petrelli et al., 2011; Petrelli et al., 2006). In many cases, mafic enclaves are envisioned to be derived from magmas that underplated a more silicic magma body and rose passively into it (Coombs et al., 2003), but they may also be injected into actively convecting magma chambers by dikes (Andrews and Manga, 2014; Hodge and Jellinek, 2012).

1.2. Summary of the 2018 Lower East Rift Zone Eruption of Kīlauea

Three compositional end-members were involved in the 2018 LERZ eruption, including the Fissure 17 andesite (MgO = 2.2 wt% whole rock), a high-Ti basalt (MgO = 4.5 wt%), and a more mafic basalt (MgO = 8.7 wt%). The high-Ti basalt and the andesite erupted mainly during the first three weeks of the eruption period, and are both thought to be derived from magma bodies within the LERZ (Gansecki et al., 2019). The high-Ti basalt may have evolved from magmas leftover in the LERZ after the 1955 eruption (Gansecki et al., 2019; Neal et al., 2019) or in the Middle East Rift Zone at some time during the 1960s (Pietruszka et al., 2021). The mafic basalt is either sourced directly from Kīlauea's summit reservoirs (Gansecki et al., 2019; Lerner et al., 2021; Mourey et al., 2023; Mourey et al., 2022), or from the Middle East Rift Zone (Pietruszka et al., 2021). The eruption was divided into five phases by Gansecki et al. (2019) based on transitions in lava compositions and eruptive behavior. Phase 1a, from May 3 to 9, involved the eruption of the high-Ti basalt end-member exclusively, from 15 separate fissure segments. This lava was relatively viscous (Gansecki et al., 2019; Soldati et al., 2021), but phenocryst-poor, and the eruption style was characterized by weak lava fountaining. Phase 1b, from May 12 to 17, also involved sporadic fountaining at low eruption rates from fissures 6, 13, 16, 18, 19, and 20 (Fig. 1). The lavas erupted during this period had compositions containing variable proportions of all three magmatic end-members: the high-Ti basalt, the mafic basalt, and the andesite. Phase 2 lasted from May 18 to 27 and involved the eruption of lavas containing all three components, but with the mafic component becoming increasingly dominant. These lavas were erupted from reactivated fissures 4, 5, 6, 8, 13, 15, 18, 19, and 20 and new fissures 21–23, and produced more extensive lava flows (USGS, 2018). The eruption of Fissure 17 occurred at the same time as phase 1b and part of phase 2, from May 13 to 25. Fissure 17 produced a 2.3 km-long blocky lava flow, a cinder cone and a series of small spatter ramparts. The westernmost segment of Fissure 17 (nicknamed the 'boomer vent' for the sound that accompanied each explosion) ejected very low volumes of bombs and emplaced a lava pad of less than 45 m in width. The most evolved lavas were andesites, erupted from the boomer vent, attaining bulk rock SiO_2 contents of 60.4 wt%. Basaltic andesites were erupted from the easternmost portion of the fissure, which produced the cinder cone and main lava flow. These lavas are thought to be a mixture of the andesite with the hybrid magma associated with phase 1b (Gansecki et al., 2019). Finally, phase 3 began on May 27th and lasted until the end of the eruption around August 4th. This phase produced the final fissure of the eruption, Fissure 24, and reactivated fissures 2, 6, 8, 13, 16, 18 and 21 (Gansecki et al., 2019; Neal et al., 2019). The lavas erupted during this phase were the mafic basalts and accounted for most of the eruptive volume ($> 1km^3$), which issued primarily from Fissure 8 (Dietterich et al., 2021). Slightly different cut-offs for the phases were proposed based on geophysical criteria by Anderson et al. (2024) that place the beginning of phase 2 on May 16th, and the beginning of phase three on May 28th. In this schema, the reactivation of fissure 20 and the opening of Fissure 24 would both be part of phase 2, but for the purpose of this paper we will categorize samples based on the geochemical criteria proposed by Gansecki et al. (2019).

2. Methods

Mafic enclaves were collected in the form of loose bombs, as nodules exposed on the surface of a ~ 4 m-wide dome-like squeeze-up, and within the Fissure 17 lava flows. Samples of Fissure 17 andesites and basaltic andesites collected include scoria from a pit near the base of the cone, lava from the boomer vent area and lava from a distal area of the main flow. Over 100 enclaves, primarily in the form of loose bombs, were acquired. New samples of the Fissure 17 lava and tephra were collected at five locations (Fig. 2a). Brief field descriptions are given in the Results section below. New samples were also collected from fissures 9–12 of the 2018 eruption (phase 1a), fissures A, M, T, U and Y of the 1955 eruption, and a variety of fissures of the 1840 and ca. 1790 LERZ eruptions (Fig. 1). Textural observations of the contact relationships between the enclaves and the host andesites were made in the field and by petrographic microscope.

2.1. X-ray fluorescence

The bulk chemistry of mafic enclave bombs and lava samples from the 2018, 1955, ca. 1790, and 1840 LERZ eruptions was determined by Wavelength-Dispersive X-ray Fluorescence at Hamilton Analytical Labs. Uncertainties are given in the Supplementary tables. New data are combined with data from Gansecki et al. (2019) and Pietruszka et al. (2021) for all phases of the 2018 and the 1960 eruption. ED-XRF data from Gansecki et al. (2019) were also integrated for mixing calculations, with their results shown on Fig. 2.

2.2. Electron microprobe analysis

Major element compositions of pyroxenes, plagioclase and olivine in samples from Fissure 17 and phase 1b of the 2018 eruption, and the 1955 and ca. 1790 eruptions were acquired using the *JEOL Hyperprobe JXA-8500F* at University of Hawai'i at Mānoa. Olivine compositions for phase 1b of the 2018 eruption were taken from Mourey et al. (2023), obtained on the same instrument. SiO_2, TiO_2, Al_2O_3, FeO, MnO, MgO, CaO, Na_2O, and K_2O were measured in all mineral phases, as well as Cr_2O_3 for pyroxene and SrO for plagioclase. The analyses were run at 15 kV and 10 nA for plagioclase using a beam diameter of 10 μm, at 20 kV and 30 nA for pyroxenes using a beam diameter of 5 μm, and 20 kV and 200 nA using a beam diameter of 10 μm for olivine. Points were taken for the core and rim of each crystal for all minerals. Estimates of precision and accuracy are given in the Supplementary tables. Elemental concentration X-ray maps of several enclaves and a crystal-rich inclusion

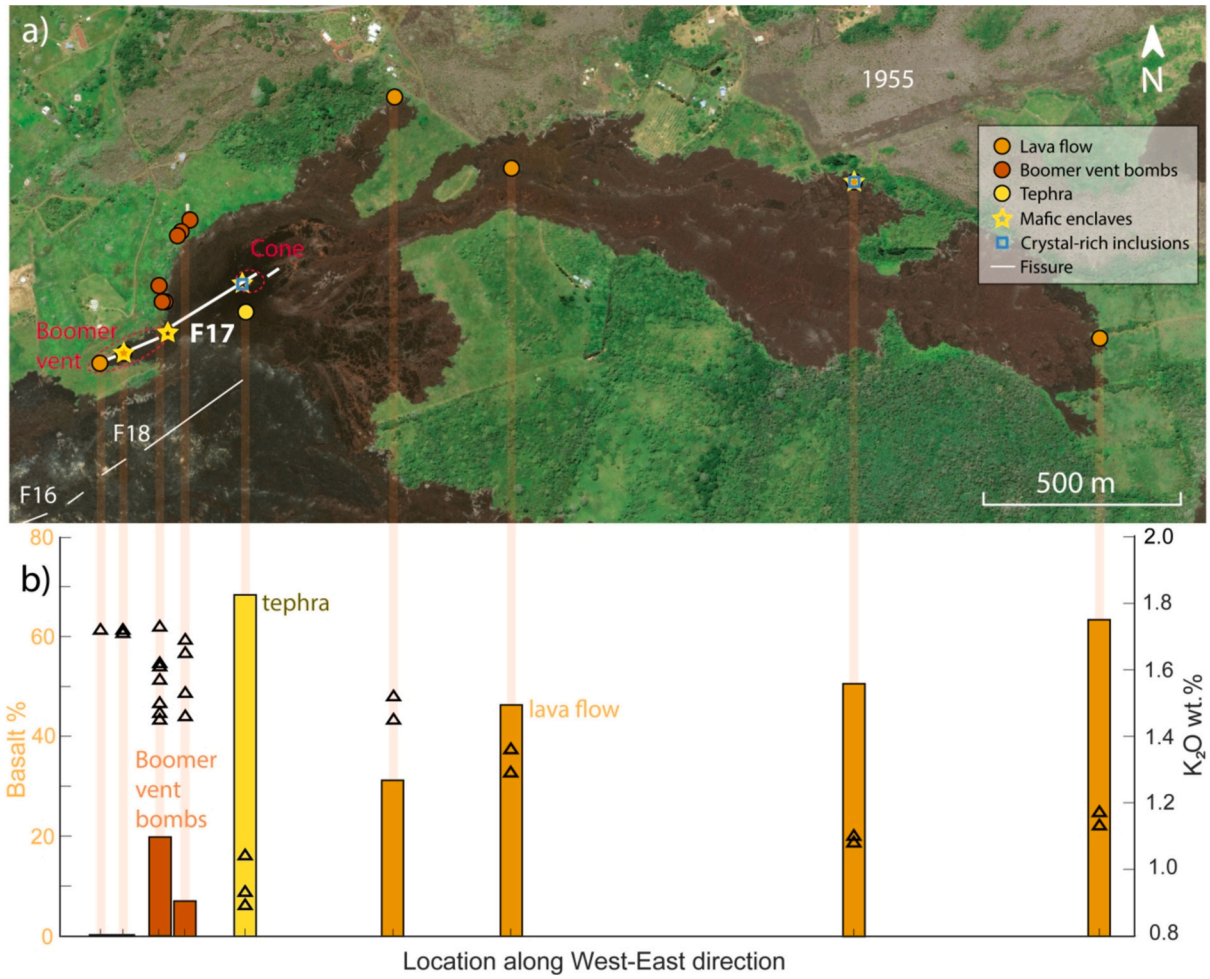

Fig. 2. a) Aerial image of Fissure 17 vents and flows with locations of samples used for geochemical characterization. b) Bars show average modeled % phase 1b basalt contribution to the bulk composition in samples at each location. Data and results for these mixing models is given in the Supplementary tables. Black triangles indicate wt% K_2O in individual samples at each location as a more direct indicator of composition.

were acquired for Mg, Ca, Si, Fe and Al at 10 kV and 300 nA. Backscattered electron (BSE) images of several enclaves and a crystal-rich inclusion were also acquired at 20 kV and 30 nA.

2.3. LA-ICP-MS

Trace element compositions of pyroxenes and plagioclase in the samples from 2018 phase 1b, mafic enclaves, Fissure 17 host lava and crystal-rich inclusions, Early 1955 and ca. 1790 were acquired using an *Analyte G2* laser ablation system with a *Thermo XseriesII Quadrupole* ICP-MS at Oregon State University. Laser spot diameters of 30 μm and repetition rates of 10 Hz were used. BCR-2G was used a calibration standard and repeat analyses were performed on BHVO-2G, ATHO-G, GSD-1G, NIST-616, StHs680-G and Menehune glass. Data was processed using the Lasertram system (Lubbers et al., 2023) and the analyses were normalized within the Lasertram software to SiO_2 using the data acquired by electron microprobe. Uncertainties are given in the Supplementary tables.

2.4. Photogrammetry and enclave image analysis

3D photogrammetric reconstructions of 50 mafic enclave bombs were carried out to characterize the range of shapes. Bombs were photographed on a rotating stand using three Nikon cameras and a TriggerBox multiple camera controller. Agisoft Metashape was used to align the photographs to generate a 3D rendering of each bomb. The stand below the bombs was manually removed from each bomb rendering within the software, and a flat surface was generated on that area of the surface of the bomb, introducing roughly 0.2 vol% error based on tests carried out with a cube of known volume. 3D images were then converted to 2D image stacks using Autodesk Netfabb and the stacks were converted to binary images in ImageJ (Schneider et al., 2012). The Matlab function 'regionprops' was used to calculate shape parameters for the three-dimensional objects including volume, surface area, solidity, convex volume and the dimensions of a best fit ellipsoid and bounding box. There is an average volume discrepancy between this method and the Archimedes method for determining volume which corresponds to roughly a 3.3 % uncertainty in axial ratios.

Enclave density in near-vent lavas at 19 locations was determined by outlining and measuring areas using ImageJ (Schneider et al., 2012) on photographs taken of subvertical exposures along the fissure. An example photograph and the corresponding set of traced enclaves used for area estimation are shown in the Supplementary information Fig. S10. Axial ratios for 2D sections of 68 enclaves from this same set of photographs were acquired using the Matlab function PARTISAN (Liu et al., 2015).

2.5. Viscosity and density estimates

The initial bulk viscosities of the mafic enclave magma and host andesite at the time of mixing, and 2018 phase 1a and phase 3 magmas, taken for comparison, were estimated by combining the models of

Giordano et al. (2008) for melt viscosity and Costa et al. (2009) to account for the effect of crystals. Vesicles were omitted from these calculations because mixing likely occurred in the magma chamber at a depth where bubbles were not yet abundant, and mafic enclaves tend to be vesicle-poor. The end-member melt compositions of the 2018 magmas were taken from the extremes of the bulk compositions (Supplementary tables). H_2O contents of 2 wt% and 1.2 wt% respectively for the andesite and the basalt were taken from volatile saturation model results in Wieser et al. (2022). Temperatures of 1132–1060 °C for the mixing scenario were calculated using the MgO-in-glass geothermometer of Helz and Thornber (1987) on end-member bulk compositions. Initial crystal contents were estimated by measuring phenocryst modal abundances in thin-sections using ImageJ (Schneider et al., 2012). For phases 1a and 3, phenocrysts were outlined manually on scanned thin-sections. For the andesite and mafic enclaves, phenocrysts were distinguished by digital area analysis of X-ray maps. The majority of the uncertainty associated with bulk viscosity calculations results from uncertainty in the melt viscosity model (up to a factor of 6.6, Giordano et al. (2008)). Density contrasts between the same compositional end-members were calculated by adding standard mineral densities to glass densities calculated using the model of Bottinga and Weill (1970) with volume and thermal expansion data from Lange and Carmichael (1987); Ochs and Lange (1999); Liu and Lange (2006) and Guo et al. (2014), and compressibility data from Kress and Carmichael (1991) and Ochs and Lange (1999). Bulk compositions were used in the calculation because glasses in samples from most eruptive phases were too microlite-rich to provide original glass compositions and phenocryst contents are typically less than 5 vol%.

2.6. Thermal conduction modeling

A 2D numerical conductive cooling model was developed to retrace the thermal evolution of a mafic enclave within the andesite magma after its incorporation in the Fissure 17 andesite. Conductive thermal equilibration between a hotter enclave and a colder host magma was modeled using Matlab. Other mechanisms of cooling are considered negligible at the scale of a single enclave. The theoretical underpinnings of this model are based on the conductive heat transfer model described in Annen (2017). Transfer of heat (Q) over space and time is written as a function of temperature and thermal conductivity (k) as:

$$\frac{\partial Q}{\partial t} = \frac{\partial}{\partial x}\left(k\frac{\partial T}{\partial x}\right) + \frac{\partial}{\partial y}\left(k\frac{\partial T}{\partial y}\right) \quad (1)$$

The heat budget Q of the enclave-host system is controlled by material density ρ, specific heat capacity C_p, temperature T, latent heat of crystallization L, melt fraction X (1- crystallinity), and thermal diffusivity K at each grid node and for each time step:

$$Q = \rho C_p T + \rho L X \quad (2)$$

where thermal conductivity and diffusivity relate to each other through:

$$k = K\rho C_p \quad (3)$$

Conductive heat transfer is modeled in two dimensions and incorporates the effect of magma composition on densities, specific heat capacity and latent heat of crystallization, and the effect of temperature on thermal diffusivity and crystallinity. Rather than focusing on the entire dike or reservoir in which magmas interacted, the model focuses on single mafic enclaves surrounded by andesite melt with the ability to control mixing fraction by modulating the size of the enclave and the size of the surrounding andesite domain. The model uses Neumann edge and corner boundary conditions to ensure that heat is conserved within the parcel of magma considered. The temperature-crystallinity relationship was based on a curve fit to the results of a MELTS model (Gualda et al., 2012), rather than a straight-line equation. The specifics and novel aspects of this model are described in the Supplementary information (Thermal conduction model). Earlier, 1-dimensional versions of the model were compared against the results of Annen (2017) to check for accuracy. The model was tested for a range of enclave sizes, determined from field observations, and local fractions of andesite and basalt magmas, derived from simple mixing calculations using bulk compositions. Values for specific heat capacity and latent heat of crystallization (Table 1) were acquired using the methods described in the Supplementary information (Calorimetry methods). Thermal diffusivities were taken from Hofmeister et al. (2016).

3. Results

3.1. Field observations

Fissure 17 lavas show a west-to-east compositional variation from andesite ('boomer vent', west) to basaltic andesite (main cone, east) along the fissure, as previously observed by Soldati et al. (2024). Mafic enclaves occur in large numbers throughout these deposits. These enclaves consist of dense, microcrystalline basalts forming dull grey masses that range from millimeters to 30 cm in diameter within the lighter, more coarsely vesicular andesite. They are found throughout the near-vent lavas, in the lava flow and as isolated bombs within the tephra of the cinder cone. The quantity of mafic enclaves in near-vent lava varies along the length of the fissure, reaching a minimum at the western end of the boomer vent, and a maximum roughly halfway along the fissure (Fig. 3). At a maximum, 6.4 % of the surface area of the near-vent lavas consists of visually identifiable mafic enclaves larger than approximately 0.5 cm in diameter. On the eastern portion of Fissure 17, mafic enclave bombs are derived from the main cinder cone and nearby spatter ramparts at the eastern end of the fissure and occur within and at the surface of the tephra deposits. They occur at a spatial density of >2 bombs per square meter on the surface of the tephra. Mafic enclaves become increasingly rare in the main Fissure 17 lava flows to the east of the cone where they make up considerably less than 1 % of surface exposures of the flow.

3.2. Textural observations

Mafic enclaves erupted as bombs generally have oblate rounded shapes and are coated in a rough, mm-scale layer of the host basaltic andesite (Fig. 4a). The distribution of axial ratios for measured enclave bombs indicates that flattened shapes are most common, where the ratio of the average minimum to maximum axis is 0.43 and the ratio of the average minimum to intermediate axis is 0.60 (Fig. 5). Visual observations confirm that the most common shapes are irregular oblate ellipsoids, including a small number of highly flattened bombs. Mafic

Table 1
Values of parameters used for thermal conduction model.

Parameter	Andesite	Enclave basalt	Source
Temperature (K)	1333.15	1405.15	Helz and Thornber (1987) thermometer
Density (kg/m^3)	2469	2642	Modified from Bottinga and Weill (1970)
Latent heat of crystallization (kJ/kg)	322.2	390.9	Emerson, 2023, Table 9
Specific heat capacity (kJ/kg*K)	1.2995	1.266	Emerson, 2023, average from Fig. 21
Thermal diffusivity parameters			Hofmeister et al. (2016), Table 6
F	2.682	7.5374	
G	0.28213	0.488	
H	11.05	19.784	
Constant K above glass transition (m^2/s)	4.20E-07	3.40E-07	

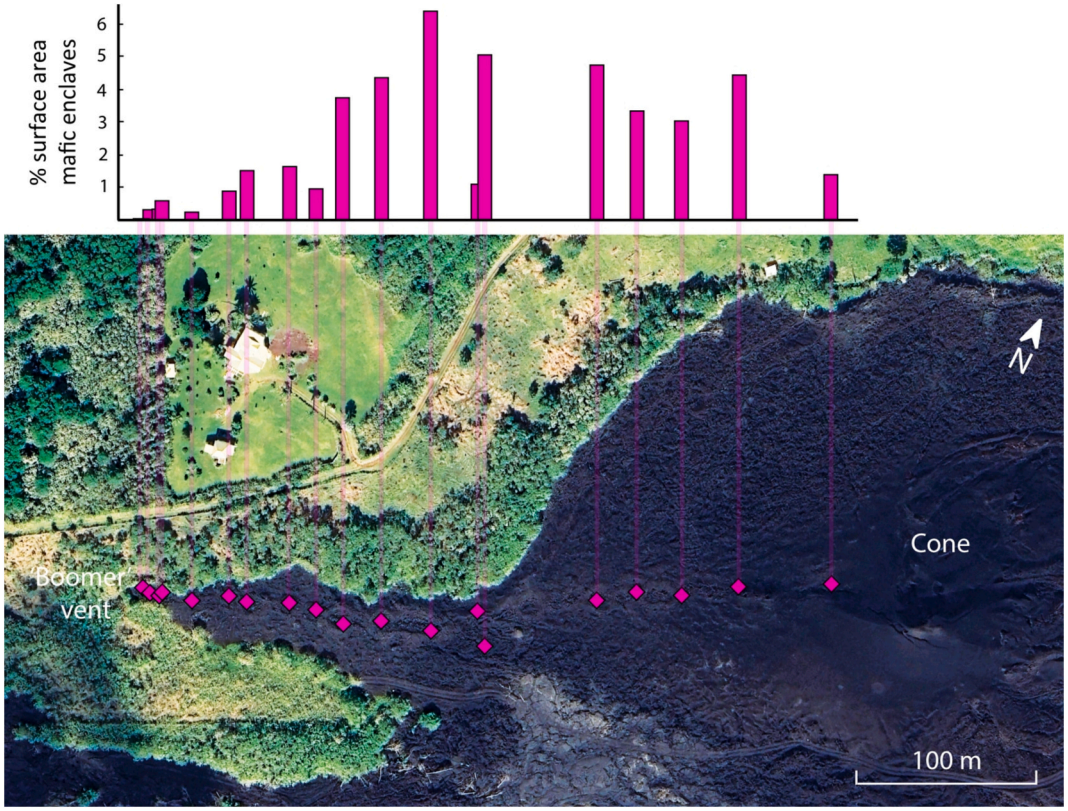

Fig. 3. Bars show the minimum surface area % of mafic enclaves within the lava flow at each marked point along the length of Fissure 17.

enclaves in the lava flows have a wider variety of shapes ranging from round to subangular to highly irregular. The smallest enclaves, on the scale of a few millimeters, are nearly ubiquitous in samples of Fissure 17 lavas. Enclaves within the lava flows can only be observed in 2D cross-sections (smooth squeeze-up or broken block surfaces). Enclaves photographed at the locations indicated in Fig. 3 show axial ratio distributions similar to the combined distribution of all 3D axial ratios (minimum:maximum, minimum:median and median:maximum together) in the enclave bombs (Fig. 5d). Our results replicate the observations of Haag et al. (2024) closely; we find axial ratios ranging from 0.26 to 0.98 in our 2D sections with a mean of 0.57 and a median of 0.56. The flow surfaces where the 2D images were taken are all subvertical sections of near-vent lavas, indicating that the enclaves are approximately randomly oriented in the areas where they are most common. By the Delesse principle, the percentage surface area of enclaves observed in these exposures should be equal to the percentage volume of the enclaves. Thus, at the point of maximum enclave density, the volume percentage of enclaves should also be approximately 6.4 %. However, this value represents a minimum, because enclaves smaller than 0.5 cm in diameter are commonly observed in thin-sections of the Fissure 17 andesite but are too small to resolve in outcrop photos.

Mafic enclaves within the lava flow display a variety of textures at the margins including highly ornate crenulate contacts (Fig. 4b, 6a, c, e), rims of finer microlites along the margin within the enclave (Fig. 6a), irregular margins on the scale of the largest groundmass microlites (Fig. 6b), and a few have patchy sections of glassy rims (Fig. 4f). The enclaves are typically microlite-rich, either holocrystalline or with only minor interstitial glass, and vesicle-poor (Figs. 4 and 6). Enclaves typically contain phenocrysts of plagioclase, clinopyroxene, and minor orthopyroxene and olivine (Fig. 6c, d), often as glomerocrysts (Fig. 6e). Enclaves can show irregular cracks partially filled with glass and vesicles running across them (Fig. 4e, 6d). Enclaves from within the lava flows sometimes have irregular, narrow, and roughly crescent-shaped voids throughout them, roughly aligned with the longest exposed axis of the enclave. These are interpreted to represent collapsed vesicles (Fig. 4c, 6c). A few enclaves contain masses of coarser crystals, glass and diktytaxitic voids which we refer to as 'crystal-rich inclusions' (Fig. 4d, 6g, h). These relatively rare crystalline masses are observed inside of the mafic enclaves as well as separately within the lava flows in a few locations. The crystal-rich inclusions are made up dominantly of elongate plagioclase and pyroxene phenocrysts; some contain plagioclase crystals up to 1 cm in length. These inclusions can contain up to 7 % Fe-Ti-oxides and 2 % apatite of phenocryst size, or at times, none of these minerals. The oxides often have ornate skeletal morphologies and frequently appear to be replacing the pyroxenes. The apatite occurs primarily as long needles (Supplementary information, Fig. S5). One observed mafic enclave has a mass of gabbro in the center of it (Fig. 6f) distinguishable from the crystal-rich inclusions by the more rounded mineral textures and presence of orthopyroxene instead of pigeonite.

3.3. Bulk compositions

Mafic enclaves have bulk compositions with 50.1 to 53.0 wt% SiO_2 and 5.72 to 6.56 wt% MgO. The Fissure 17 andesites and basaltic andesites range from 53.1 to 60.4 wt% SiO_2, similar to the results of Soldati et al. (2024) (52.6–61.2 wt% SiO_2 and 2.26 to 5.08 wt% MgO). Crystal-rich inclusions have bulk compositions that are controlled by accessory phases that they contain in large proportions, including apatite and Fe-Ti-oxides and thus are not shown in Fig. 7. Major element compositions of the mafic enclaves range from typical Kīlauea rift basalts to slightly more evolved compositions, but with slightly more scatter, particularly in TiO_2. The more evolved enclaves trend not in the direction of Kīlauea's typical crystal fractionation trend (determined empirically from a compilation of whole rock analyses from Kīlauea) towards high-Ti basalts, but in the direction of the suggested mixing trend between phase 1b, itself a mixture of phase 1a and 3, and the most evolved Fissure 17 andesite (Fig. 7).

The mixing relationship for the products of Fissure 17, proposed in

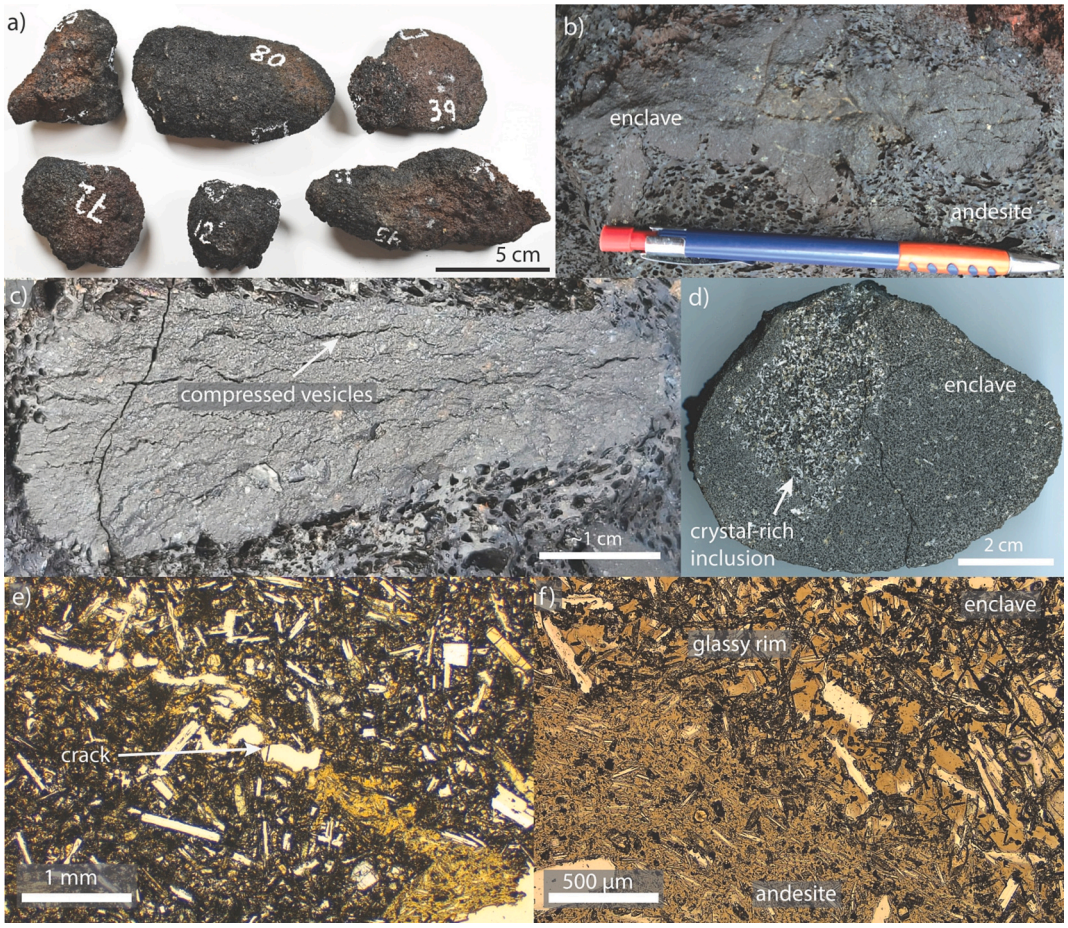

Fig. 4. Field, hand sample, and petrographic images of mafic enclaves. a) Enclave bombs collected from the surface of the tephra blanket showing a range of typical geometries, from rounded to more irregular shapes and from equant to more elongate. b) Enclave in near-vent lavas of the boomer vent with crenulate margins. c) Enclave in near-vent lavas of the boomer vent with compressed vesicles. d) Enclave bomb cut to reveal a crystal-rich inclusion inside. e) Petrographic image in plane-polarized light showing an irregular crack at the edge of an enclave with host andesite inside. f) Petrographic image in plane-polarized light showing the contact between an enclave and the host andesite with a rare glassy rim.

Gansecki et al. (2019) is further supported by our data. The phase 1b sample that falls towards the andesite along this trend in our data is from Fissure 13, interpreted by Gansecki et al. (2019) to represent leakage of Fissure 17 andesite into the main fissure system. Treating the extreme compositions of the andesite and phase 1b basalts as mixing end-members, the andesites and basaltic andesites samples represent mixtures with 0 to 74 % phase 1b basalt. Samples of lava from the western end of the boomer vent form the pure andesitic end-member. Andesite bombs ejected from the boomer vent contain estimated basalt contributions ranging from 0 to 34 %. Tephra samples from the cinder cone, taken at the surface and the bottom of a pit dug to the level of the lava flow, have the greatest basalt contribution to the bulk composition, roughly 74 %, and samples from the main Fissure 17 lava flow range from 31 to 65 % basalt. Fig. 2b shows the spatial distribution of these mixtures, incorporating additional ED-XRF data on the same samples from Gansecki et al. (2019), while Fig. 7 shows more detailed compositional information.

Whole rock compositions of lavas from the Early 1955 and ca. 1790 eruptions were analyzed to test the possible hypotheses for the enclaves' origins. The Early 1955 lavas are high-Ti basalts which are more similar to phase 1a lavas of the 2018 eruption than phase 1b or the enclaves. The compositions shown, from lava and tephra produced in 1955, should be representative of any potential 1955 xenoliths. Any 1955 magma stored in the rift zone and remobilized in 2018 might be even more evolved in composition. Whole-rock samples from the ca. 1790 eruption have a wide range of compositions (5.76 to 9.07 wt% MgO) with the most evolved samples being similar in composition to some of the enclaves and phase 1b, and the least evolved being more mafic than phase 3 of the 2018 eruption. We have no samples from the ca. 1790 fissure closest to Fissure 17, and it is now mostly buried beneath the 2018 lava flows in the area of Fissure 20. The nearest sample of ca. 1790 (S9 in Fig. 1) is one of the most mafic we analyzed (8.82 wt% MgO). The composition of magmas that remained and evolved in the rift zone following the ca. 1790 eruption by 2018 depends on the rate of cooling of the magma body, which is unknown, but the direction of chemical differentiation would at least be *towards* that of the least evolved enclaves. The other two historical LERZ eruptions, the 1840 and 1960 eruptions, and the late stage of the 1955 eruption are shown for comparison, but considered unlikely to be possible sources of the enclaves because their fissures are too far away. In addition, the 1840 eruption produced distinctive olivine-rich picrites in the LERZ (Moore and Trusdell, 1991).

Incompatible element ratios like Nb/Y ratios are useful indicators of magmatic sources at Kīlauea because they are largely insensitive to crystal fractionation. Nb/Y ratios in lavas erupted at the summit vary in a cyclical pattern that has been relatively well characterized for the last ~200 years of Kīlauea's eruptive history (Garcia et al., 2003; Pietruszka and Garcia, 1999). In rift zone lavas, this ratio can provide temporal constraints on when the magma was emplaced into the rift zone by connecting it with a period of summit magmatism and is thus helpful for distinguishing stored magmas emplaced at different times (Pietruszka et al., 2021; Wieser et al., 2022). Whole rock Nb/Y in the mafic enclaves ranges from 0.55 to 0.65 while the Fissure 17 host lavas range from 0.58

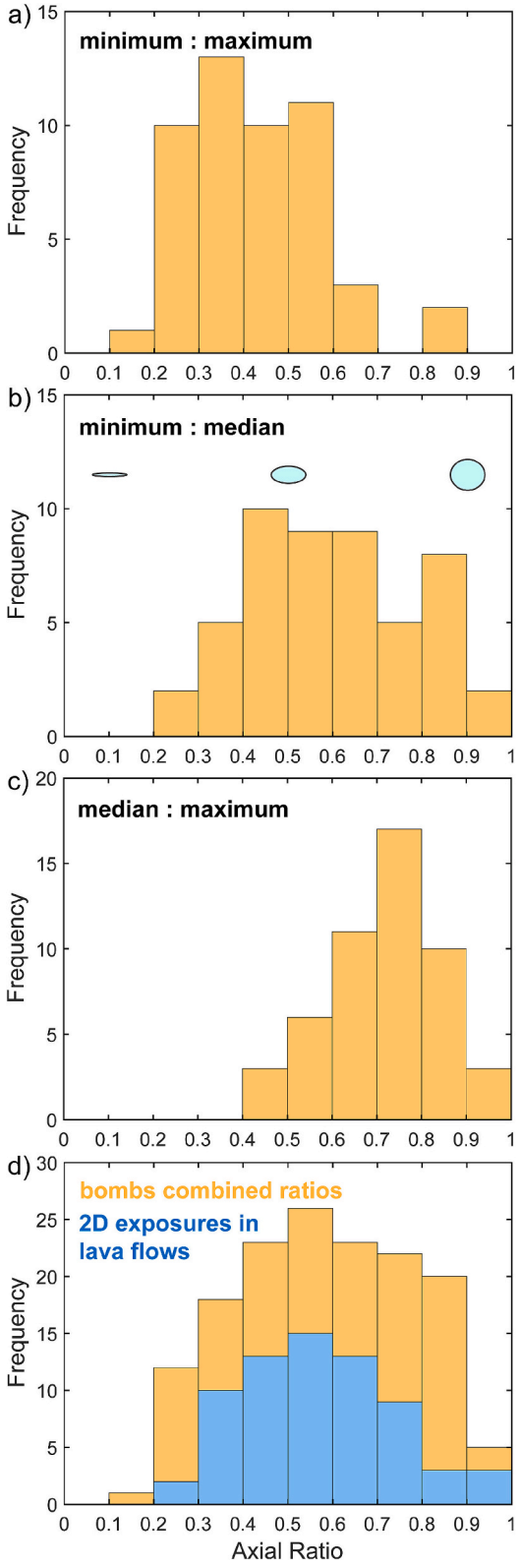

Fig. 5. Histograms of mafic enclave morphology expressed as axial ratios. Pale blue ellipsoids provide a visual reference for the shapes the ratios. Axial ratios in enclave bombs are given for a) minimum:maximum, b) median:maximum, c) median:maximum, and d) all combined axial ratios in the mafic enclave bombs and minimum:maximum axial ratios in natural 2D exposures of mafic enclaves within the boomer near-vent lavas. (For interpretation of the references to colour in this figure legend, the reader is referred to the web version of this article.)

to 0.71. Overall, throughout the 2018 eruption, the Nb/Y ratios dropped with time starting at a maximum of approximately 0.74 during the first few days of the eruption to values as low as 0.45 at the very end of the eruption three months later, marking the transition from older rift magmas to recent mafic inputs from the summit (Fig. 7). The Nb/Y ratios of the enclaves and Fissure 17 lavas are both consistent with this trend and are similar to the values found in the contemporaneously erupting phase 1b basalts, which have Nb/Y from 0.58 to 0.62 (Fig. 7d). The most evolved unmixed andesites have the highest Nb/Y ratios in the Fissure 17 system (0.69 to 0.71). The enclave Nb/Y ratios are generally lower than in lavas from the 1955 eruption, but there is overlap with the set of Early 1955 samples collected from vent U on the southern fissure alignment, which had Nb/Y values of 0.64 to 0.65. Samples from vents A and M on the northern fissure alignment close to Fissure 17 had Nb/Y of 0.72 to 0.73. Samples from the ca. 1790 eruption show strong overlap in the opposite direction, having a range of Nb/Y values from 0.50 to 0.61.

3.4. Mineral compositions

Mafic enclaves contain on average 5 vol% phenocrysts of plagioclase (~3.6 %), clinopyroxene (~1.3 %), olivine (~0.1 %), and orthopyroxene (~0.1 %). The crystal-rich inclusions contain plagioclase, clinopyroxene, pigeonite, apatite, and Fe-Ti-oxides. The host andesite contains phenocrysts of plagioclase and clinopyroxene with very minor pigeonite, orthopyroxene, and olivine, for a total of around 2 vol% phenocrysts on average. The major element compositions of phenocrysts in all basalt materials analyzed largely overlap. The averages and ranges of clinopyroxene compositions in Early 1955, ca. 1790, and phase 1b lavas and the mafic enclaves are not meaningfully distinguishable. Orthopyroxene in mafic enclaves and phase 1b samples share the same peak at $En_{73.5}$, although one enclave was also found to contain a single pigeonite phenocryst. The Early 1955 low-Ca pyroxenes have a greater average En ($En_{48.7}$) and also include a few pigeonites, while the ca. 1790 orthopyroxenes skew to higher En values, with an average of $En_{50.2}$. Olivine phenocrysts in phase 1b and the mafic enclaves share nearly identical distributions of Fo, with means of $Fo_{77.4}$ and $Fo_{77.2}$ respectively. Early 1955 olivines are similar in their most dominant compositions, with an average of $Fo_{78.6}$. However, it should be noted that olivine phenocrysts in the Early 1955 samples were exclusively observed at Fissure U, on the southern fissure line roughly 11.3 km away from Fissure 17. These 1955 olivines also generally show disequilibrium textures not observed in the other basalts. The ca. 1790 samples, which contain a much greater abundance of olivine phenocrysts have a slightly higher average Fo ($Fo_{80.1}$). Plagioclase compositions differ the most between the different basalt samples. Phase 1b has a distinct secondary peak at around An_{48} in phenocrysts originating from Fissure 13 (Fig. S7 in Supplementary information shows the differing mineral distributions from the two samples, which appear to reflect the differing magma contributions as shown in the bulk data (Fig. 7)). The mafic enclaves and Early 1955 plagioclase both show similar-looking compositional peaks, at approximately An_{65} and a less substantial tail of lower An values. The ca. 1790 plagioclase is noticeably more anorthite-rich ($An_{72.7}$ on average) and shows no low-An tail.

The Fissure 17 lavas and the crystal-rich inclusions have dominantly low-An plagioclase, although the lavas have more of a high-An tail. The crystal-rich inclusions and the host lavas also share similar low-Ca pyroxene compositions, dominantly pigeonites instead of the orthopyroxene that is found in the basalts (Fig. 8b). The distribution of clinopyroxene compositions in the host andesites resembles neither that of the crystal-rich inclusions nor any of the basalts but appears to be a possible amalgamation of both distributions (Fig. 8a). No olivine is present in the crystal-rich inclusions. The compositions of the small quantity of olivine present in the andesites match the distribution of Fo values in the enclaves and the phase 1b basalts (Fig. 8c). Fig. S7 in the Supplementary information shows that there is minimal difference between phenocrysts in host lava samples from the boomer vent and distal

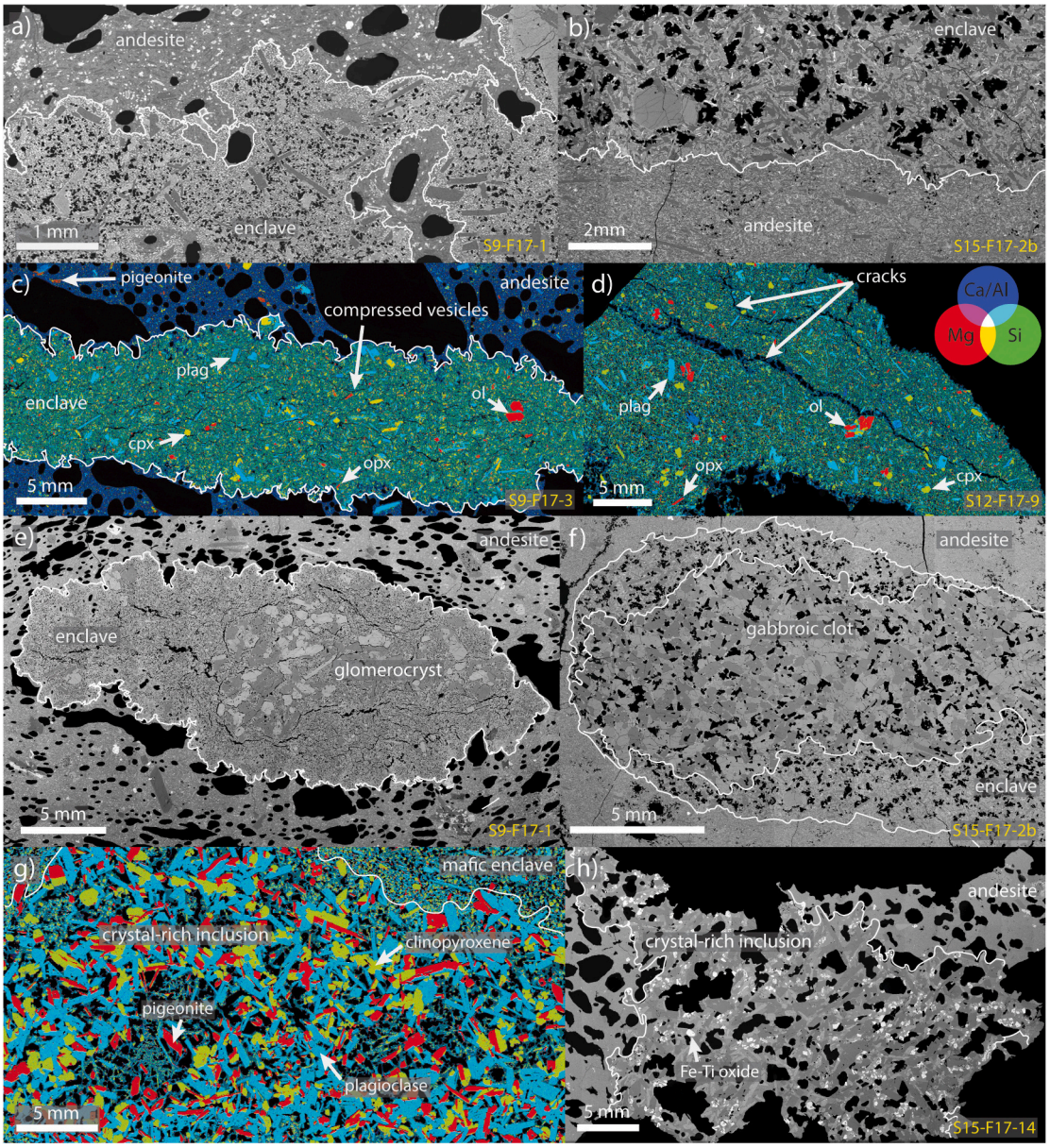

Fig. 6. Images of various enclave and crystal-rich inclusion features in BSE images and X-ray major element maps. The X-ray maps are composed of Mg, Si and Ca/Al maps in RGB. Bright red minerals are olivine, dark red minerals are low-Ca pyroxene, yellow-green minerals are clinopyroxene, and blue minerals are plagioclase. A) BSE image of an enclave margin showing a crenulate and intermingled texture with finer microlites at the contact. B) BSE image of an enclave margin with an irregular contact with the host andesite but no marked difference in enclave texture at the edge or interior. C) X-ray map showing an enclave in near-vent lavas with compressed vesicles and a typical assemblage of olivine, plagioclase, and clinopyroxene. D) X-ray map of a portion of an enclave bomb with a thin rim of basaltic andesite and irregular cracks partially infilled by basaltic andesite. E) BSE image of a small enclave with crenulate margins, collapsed vesicles and a large glomerocryst in near-vent lava of the boomer vent. F) BSE image of a small, rounded enclave containing a large mass of gabbro taken from the distal Fissure 17 lava flow. G) X-ray map of a portion of a crystal-rich inclusion inside of a mafic enclave. H) BSE image of a portion of a crystal-rich inclusion in the host lava showing the quantity of large Fe-Ti-oxides. (For interpretation of the references to colour in this figure legend, the reader is referred to the web version of this article.)

flow. In the crystal-rich inclusions, pigeonite and clinopyroxene are found as zones in individual crystals and separately. The zones may be concentric or irregular, and the pigeonite is more commonly but not exclusively found in the cores of concentrically zoned crystals. This zoning is also observed in a small number of crystals in the andesite. The rare olivine phenocrysts in the andesite display disequilibrium textures such as resorption and reaction rims, indicating that they are not in chemical equilibrium with the andesite (Fig. S6, Supplementary information). MELTS (Gualda et al., 2012) models suggest that no olivine would crystallize from the andesite bulk composition at the expected temperature (roughly 1060 °C for the andesite using the Helz and Thornber (1987) MgO thermometer) and pressure (64 MPa based on saturation pressure estimates from Wieser et al. (2022)). Some plagioclase phenocrysts in the andesite also show disequilibrium textures, including high degrees of rounding, formation of a rim, and in a few cases, sieve textures.

A ratio-ratio plot of Ba/Sr vs La/Eu in plagioclase (Fig. 9a) provides an example of trends that are observed in plots of all trace elements and their ratios in plagioclase. Plagioclase in the Fissure 17 lavas forms an extensive compositional trend in the direction of increasing Ba/Sr. This trend is likely controlled by the extent of plagioclase fractionation at the time of phenocryst formation since fractionation is typically the strongest control on Sr concentration. The crystal-rich inclusions form a compositional population that is a narrow subset of those seen in the

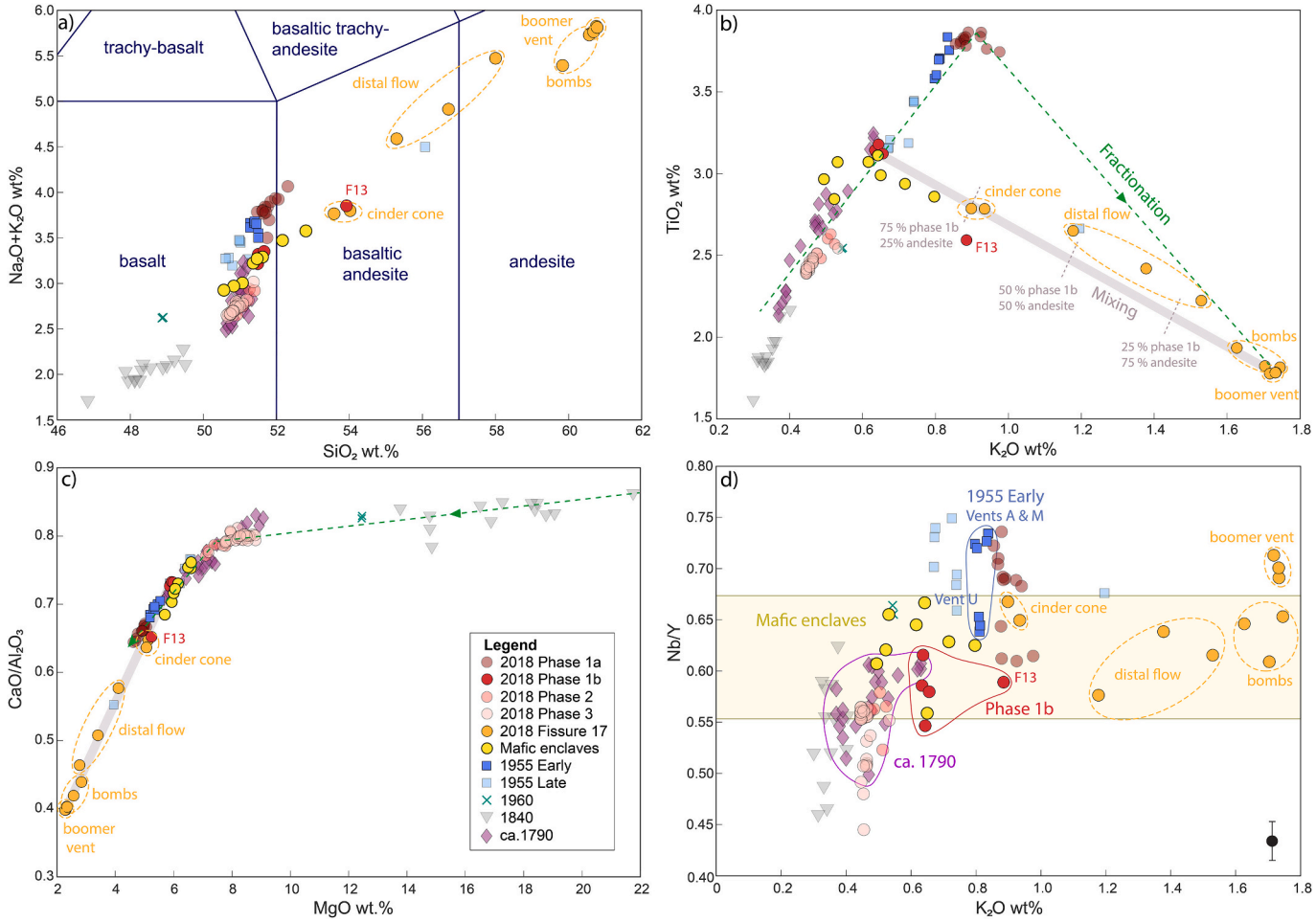

Fig. 7. Bivariate plots showing some key elements for bulk compositions of all historical LERZ eruptive products. Errors in the major elements are smaller than point size, an average error of one standard deviation in Nb/Y is shown. Green dashed lines indicate the approximate all-Kīlauea fractionation trend and grey lines indicate the mixing trend between phase 1b and the most evolved andesite. The calculation of the mixture between the least evolved phase 1b sample and the most evolved andesite required to produce each of the samples of Fissure 17 lava represented here and in Fig. 2b is shown in the Supplemental tables. Data from different parts of the Fissure 17 system are distinguished with dashed outlines. New data is combined with data from Gansecki et al. (2019) and Pietruszka et al. (2021). An anomalous bulk composition for phase 1b from Fissure 13 is indicated on all plots as F13. (For interpretation of the references to colour in this figure legend, the reader is referred to the web version of this article.)

andesite but is not an end-member of the trend. The gabbroic clot observed inside one enclave contains a very distinct plagioclase population. The four basalts considered, 2018 phase 1b, Early 1955, ca. 1790, and the mafic enclaves, have very similar trace element populations in plagioclase. However, the phase 1b lavas and enclaves have the most similar distributions, including a narrow main compositional cluster and a smaller set of data points at higher Ba/Sr and lower La/Eu within the trend defined by the andesite-hosted plagioclase. Correspondingly, a portion of the andesite-hosted plagioclase falls within the geochemical cluster defined by the basalts.

Clinopyroxene trace element data forms two primary populations, one dominated by the crystal-rich inclusions with a small number of phenocrysts from mafic enclaves and the andesite, and another encompassing all other clinopyroxenes in both basalts and andesites. Fig. 9d shows an example of the pattern that is observable in most element-element and ratio plots of trace elements in clinopyroxene. The trace element compositions of each sample set are highly diverse. Clinopyroxenes in the crystal-rich inclusions have a very narrow compositional range and are substantially more enriched in most trace elements, and particularly in the most incompatible elements (Supplementary information, Fig. S8). A small number of clinopyroxenes in the mafic enclaves share similar compositions to the clinopyroxenes in the crystal-rich inclusions. Clinopyroxenes from phase 1b and the mafic enclaves share a high V/Y population not observed in the other analyzed lavas (Fig. 9c) and the Early 1955 samples contain a high LREE/Y population (Fig. 9b) not observed in the other materials. Clinopyroxene phenocrysts in the ca. 1790 samples have very similar trace element compositions to both the other sample sets but tend to show more scatter. Orthopyroxenes, while present (Fig. 8) were not successfully analyzed in the mafic enclaves by LA-ICP-MS, but all other considered populations were. Fig. S9 in Supplementary information shows similar orthopyroxenes in phase 1b and Early 1955, limited inconclusive data for ca. 1790, and distinct orthopyroxene populations for the gabbroic clot and the crystal-rich inclusions.

3.5. Viscosity and density estimates

The measured mafic enclaves have a bulk density range of approximately 2660–2690 kg/m^3 based on the range of observed crystal contents. The bulk density of the most evolved andesite has a range of approximately 2490–2530 kg/m^3. The maximum density contrast between the andesite and the mafic enclave magmas is 205 kg/m^3 using the minimum observed phenocryst content for the enclaves and maximum for the andesite. The reverse scenario yields a minimum density contrast of 140 kg/m^3. For comparison, the bulk densities of the two extreme basaltic end-members of the 2018 eruption are 2690–2730

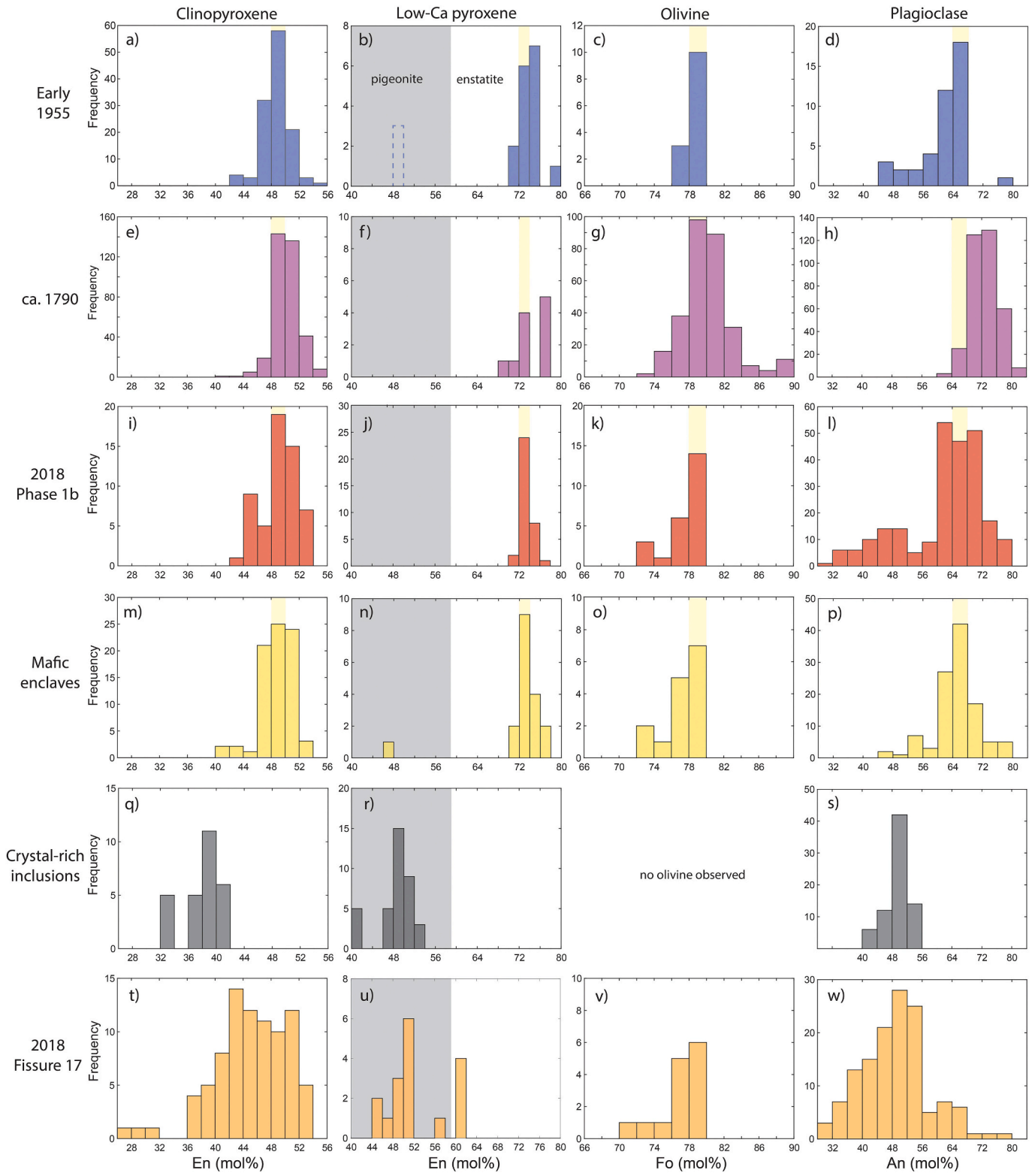

Fig. 8. Histograms of clinopyroxene, low-Ca pyroxene, olivine and plagioclase phenocryst compositions in a-d) Early 1955 lavas, e-h) ca. 1790 lavas, i-l) phase 1b lavas, m-p) mafic enclaves, q-s) crystal-rich inclusions, and t-w) Fissure 17 host lavas. The dashed bar in b) represents three pigeonites observed during LA-ICP-MS that were not analyzed by electron microprobe. An additional row of plots for the gabbroic clot found in the enclave in Fig. 6f is shown in Supplementary information Fig. S7. The host Fissure 17 andesite additionally contained one large fayalite with Fo_{33} not shown on this diagram.

kg/m^3 for the phase 3 mafic end-member and approximately 2660 kg/m^3 for the phase 1a high-Ti basalt, giving a maximum density contrast of almost 80 kg/m^3 if the minimum crystal content is used for phase 1a and the maximum for phase 3, and a minimum of 30 kg/m^3 for the reverse scenario. Most of this difference is associated with the variability in the crystal content of phase 3 samples.

The modeled viscosity of the mafic enclave magma ranges from 64 to 86 Pa s using a calculated temperature of 1135 °C for a typical mafic

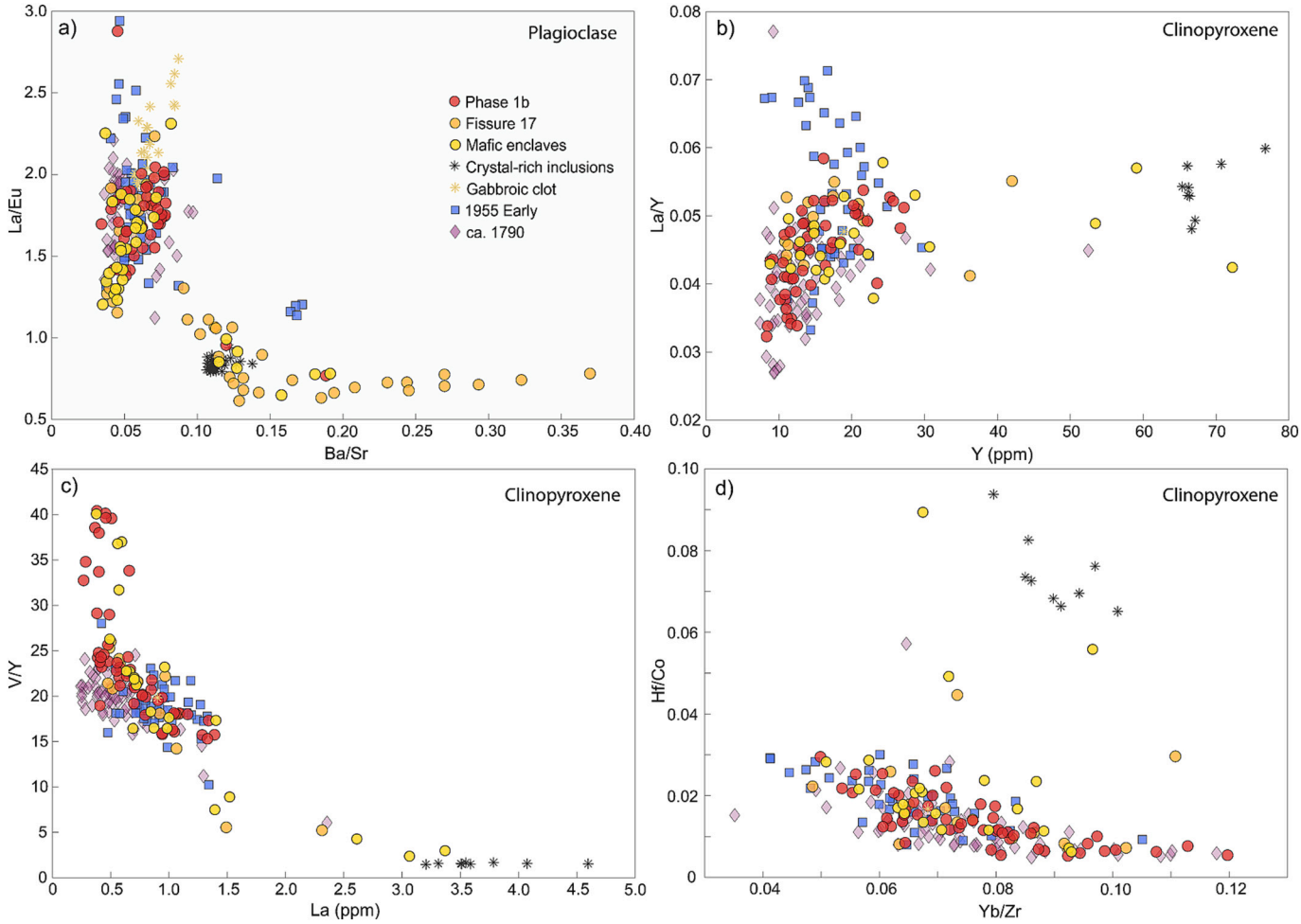

Fig. 9. Bivariate plots of trace element ratios useful for distinguishing mineral populations in phenocrysts from mafic enclaves, crystal-rich inclusions, host andesite, 2018 phase 1b, and Early 1955 lavas, in a) plagioclase and b) through d) clinopyroxene.

enclave bulk composition and a crystal content of 1.5 to 12 vol%. The host andesite has modeled viscosities ranging from 784 to 826 Pa s at 1061 °C for phenocryst contents of 1 to 3 vol%. Therefore, the mafic enclave magma and the andesite would have an initial viscosity contrast of 698 to 763 Pa s (or a ratio of ~9–13). The range of modeled viscosity values for the andesite is lower than those measured by Soldati et al. (2024) at 1172 °c. This suggests that our viscosity values may be low overall, and thus our viscosity differences between mixing phases may be underestimates. The viscosity of the phase 1a mixing end-member for the eruption ranges from 172 to 190 Pa s given approximate crystal contents of <1 to 4 vol%. The viscosity of the phase 3 end-member is 30 to 32 Pa s given approximate crystal contents of 2.5 to 5 vol%. We calculate that the two basaltic end-members of the eruption, the phase 1a and phase 3 magmas, had an initial viscosity contrast of 139 to 160 Pa s (or a ratio of ~6).

These observations are in line with the model of Semenov and Polyansky (2017) which suggests that magmas with a density contrast of >100 kg/m^3 will primarily mingle, in this case the enclave and andesite magmas, while magmas with lesser density contrasts should mix and homogenize, in this case the phase 1a and phase 3 end-members. Their model suggests that viscosity primarily controls whether mingling melts interpenetrate or form rounded droplets within each other.

4. Discussion

4.1. The nature and source of mafic enclaves in the Fissure 17 andesite

Investigating the origin of mafic enclaves observed within the andesites and basaltic andesites of Fissure 17 requires answering two questions: 1) Were these basaltic masses incorporated into the host lava in solid or molten form? 2) Were the enclaves sourced from the same 2018 phase 1b basalt that intruded, remobilized, and mixed with the andesite magma body to produce the less evolved products of Fissure 17, or were they sourced from another nearby stored magma? Magma thought to have been stored in the LERZ since 1955, or an earlier eruption thought to have occurred in approximately 1790, were considered as potential alternative sources for the enclaves. The typical rounded shapes of the enclaves, as well as the presence of highly crenulate margins (Figs. 4 and 6) and partially glassy rims on some enclaves (Fig. 4), suggest that the basalt was partially molten at the time of contact with the andesite and initially behaved as a viscous fluid. Compressed vesicle shapes in some enclaves further support the suggestion that the enclaves were still sufficiently fluid to vesiculate and subsequently deflate following introduction into the andesite. The mafic enclaves are nearly holocrystalline, while the host lava has a substantially glassy groundmass which indicates that the enclaves did not fully quench on contact with the andesite. However, the presence of irregular andesite-filled cracks in a few enclaves suggests that the enclaves became relatively rigid due to microlite crystallization, while the andesite was still able to flow. While in the conduit or lava flow,

enclaves appear to have responded to strain in a semi-brittle fashion while the host lava was still sufficiently fluid to flow into the cracks, and perhaps dismantle some enclaves to produce rare subangular faces.

The presence of similar crystal-rich inclusions both within the lava flow and inside some mafic enclaves, as well as the gabbroic clot inside one enclave, which appears to be a xenolith unrelated to any of the analyzed magmas, support the idea that the enclave-forming magma was partially molten rather than solid at the time of contact. We suggest that the crystal-rich inclusions represent samples of a crystal mush with low melt fraction, related to or closely adjacent to the andesite magma chamber. They might be derived from a portion of the mush pile of the andesite body that became isolated after protracted differentiation, and was in chemical disequilibrium with the melt-rich upper portion of the magma body. Alternatively, they may be derived from a small, isolated, highly differentiated, and extensively crystallized magma body unrelated to the andesite located between Fissure 17 and the neighboring fissures 16 and 18 that intruding lava mobilized en route to Fissure 17. Soldati et al. (2024) suggested the stored magma from 1955 as the source of the crystal-rich masses and many of the crystals in the andesite, but our data does not support this hypothesis. In either scenario, pieces of what may have been a continuous layer would have been mobilized and sometimes engulfed by the intruding basalt.

Major element bulk compositions of the enclaves show compositions that range from typical Kīlauea rift zone basalts to more evolved basalts along the less typical trend formed by the basaltic andesites and andesites at Fissure 17. Major and trace element compositions of phenocrysts in the Fissure 17 lavas show that minerals that formed in the andesite and the crystal-rich inclusions are also present within the enclaves. Some of the increased scatter in the enclave compositions, particularly in TiO_2, may be the result of incorporation of crystal-rich inclusions or some of their phenocrysts into some enclaves. Evidence of incorporation of phenocrysts from the andesites includes the presence of pigeonite, and secondary populations of low-An, low La/Eu and high-Ba/Sr plagioclase and high La, Y and Hf/Co clinopyroxenes in the enclaves. Several of these observations are also true of the phase 1b basalts. Gansecki et al. (2019) suggested that phase 1b magmas consisted of various mixing proportions of phase 1a, and phase 3 magmatic end-members with a more minor fraction of Fissure 17 magma that leaked into the main fissure trend. The products of Fissure 17 show more compositional variability, but with the andesitic component being the dominant component and the mixture of phase 1a and phase 3 (phase 1b) being the minor end-member. This binary mixing scenario was tested with the whole rock data compiled from our study and Gansecki et al. (2019), and found to yield reasonable results (Figs. 2, 7, and Supplementary tables). Thus, the mafic enclaves must have either undergone the same process as phase 1b (mixing with the andesite component and mineral exchange), or they must *be* phase 1b. The phase 1b basalts have an overlapping range of bulk compositions and contain mineral populations not meaningfully distinguishable from the mafic enclaves. This includes, in particular, a population of high V/Y clinopyroxenes only observed in these two materials. Lavas erupted in early 1955 and roughly 1790 from nearby vents have similar mineral compositions to both the enclaves and phase 1b, as well as strongly overlapping whole rock Nb/Y values. Magma left behind in the rift zone following these eruptions would have evolved an unknown amount during the interceding period. The Early 1955 magma, being more evolved than the enclaves, could not have differentiated to match the enclave compositions. Compositional indicators not affected by fractionation are most useful for evaluating the similarity of the magma that would have been present in these bodies in 2018. The traditional criteria of whole rock Nb/Y is ambiguous for all of the considered options. Trace element concentrations in minerals show slightly different, but substantially overlapping compositional populations with both the 1955 and ca. 1790 samples. The ca. 1790 phenocrysts cover a broader compositional range in some elements.

The simplest scenario for the formation of the enclaves is that they consist of the phase 1b magma already proposed to have intruded the Fissure 17 magma chamber, but a portion that was unable to homogenize and formed isolated masses instead. Importantly, a phase 1b origin for the mafic enclaves does not rule out any involvement of Early 1955 magma. Rather, it rules out its direct involvement without mixing first in a partially molten state with phase 3 and Fissure 17 magmas. In other words, leftover 1955 magma could be the source of the high-Ti phase 1a magmatic end-member prior to mixing with other magmas in 2018, as was suggested by Gansecki et al. (2019). We thus make the important distinction that the mafic enclaves may be partially derived from the magmas involved in the early phase of the 1955 eruption, but cannot consist of that magma *alone* as proposed by Haag et al. (2024). We must then consider how phase 1b basalt might have interacted with the andesite magma body to produce both fully homogenized basaltic andesites containing rare enclaves, and andesites preserving numerous mafic enclaves, along a fissure less than 0.5 km in length. The following sections address the mechanisms and timescales associated with magma mixing and enclave preservation necessary to answer this question.

4.2. Thermal conduction model results

A series of 2D thermal conduction models were run to simulate a realistic range of mingling scenarios for an elliptical mass of enclave magma surrounded by Fissure 17 andesite magma. Enclaves with realistic aspect ratios of approximately 0.4 and major radii between 1 and 15 cm were tested. By changing the size of the enclave and numerical domain, mixing fractions of basalt ranging from 1 to 50 vol% were explored. We define the thermal equilibration timescale (t_e) as the time by which the difference between the maximum and minimum temperature values in the system becomes less than 1 °C. The final thermal equilibration temperature was largely controlled by the mixing fraction, while the time to reach the equilibrium temperature was more strongly dictated by the size of the enclave (Fig. 10). Time t_e was reached most quickly for small enclaves and larger fractions of basalt in the system. For the smallest enclaves (1 cm major semi-axis radius in the model), equilibrium could be reached in minutes, while the slowest feasible scenario yielded 10 days for an enclave with a major semi-axis radius of 15 cm to re-equilibrate in a system with 1.1 vol% basalt (Fig. 10a).

Models and experimental data for the effect of crystals on the viscosity of suspensions all show rapid increases in bulk viscosity of several orders of magnitude at crystal fractions between 40 and 60 vol% (Costa et al., 2009; Lejeune and Richet, 1995; Mader et al., 2013; Namiki and Tanaka, 2017). At the higher end of this range, the magma undergoes rheological locking with crystals impinging on one another and forming a semi-rigid framework that prevents efficient magma mixing and results in the preservation of enclaves. Given the wide range in experimental data, we consider enclave preservation to require somewhere between 40 and 60 % crystallinity. Our MELTS (Gualda et al., 2012) model results suggest that the phase 1b basalt would attain roughly 59 % crystallinity at the temperature of the Fissure 17 andesite; therefore the rheological locking crystallinity must necessarily be less than 59 % for the enclaves to have formed. In our cooling models, 40 % crystallinity is reached for all scenarios with <38 vol% basalt, at 1099 °C. The largest modeled enclaves reached this threshold after approximately 24 h. Up to 6.4 vol% of enclaves are observed in the boomer vent lava flows. A model run with close to this percentage of basalt, 6.8 %, reaches a maximum crystallinity of approximately 55 % after equilibration. This result suggests that the minimum crystallinity required for enclave preservation cannot be more than about 55 % (Fig. 10). The largest modeled enclaves took approximately 62 h to equilibrate in the 6.8 % basalt scenario. At all basalt fractions, the smallest enclaves modeled, 1 cm diameter, equilibrate in less than four minutes.

4.3. Magma interaction mechanisms

The low vesicularity of the mafic enclaves suggests active intrusion

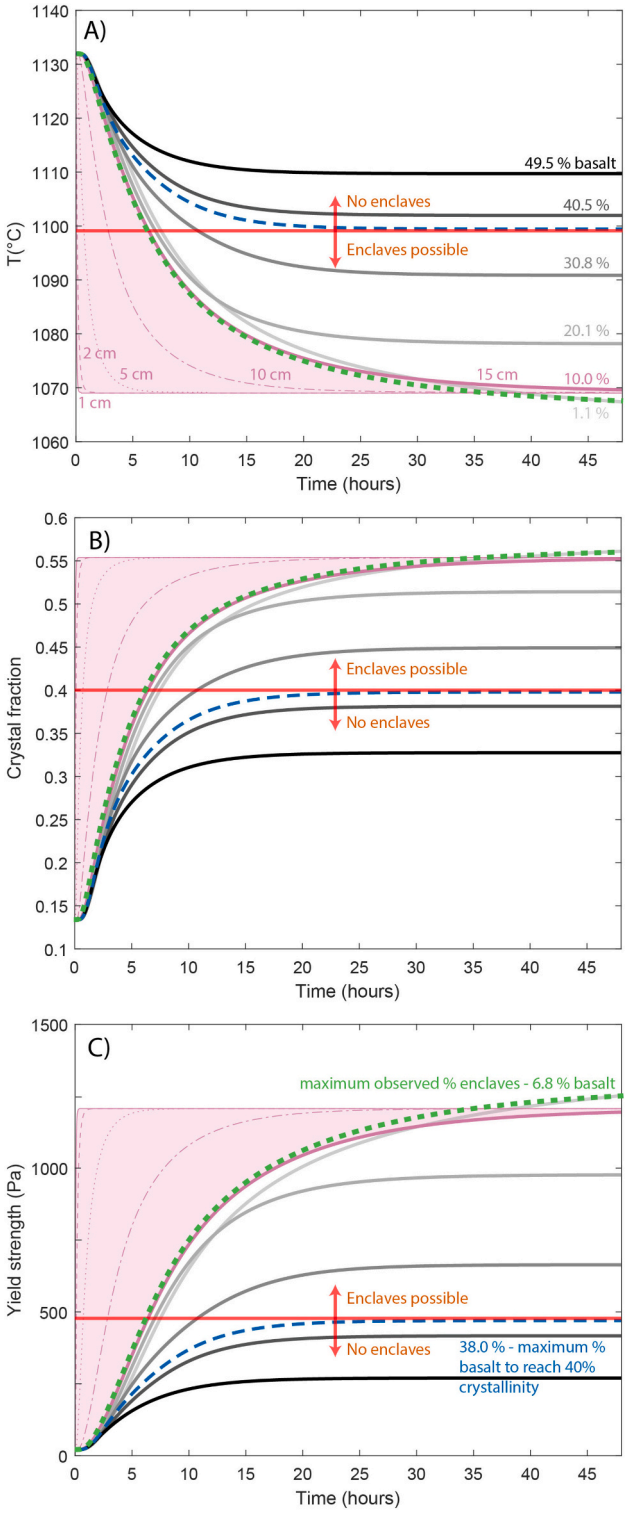

Fig. 10. Plots showing the results of thermal conduction models for the equilibration of an elliptical volume of phase 1b basalt in Fissure 17 andesite. Solid lines show the slowest equilibration scenario, involving the largest modeled enclave with a maximum radius of 15 cm, for various volume % of basalt. The pink zone shows the results of equilibration for enclave sizes ranging from a maximum radius of 1 cm to 15 cm in a 10 vol% basalt scenario. A) Change in temperature at the center of the modeled basalt region with time. B) Change in crystallinity at the center of the modeled basalt region with time. C) Change in yield strength at the center of the modeled basalt region with time using the equation of Dragoni (1989). (For interpretation of the references to colour in this figure legend, the reader is referred to the web version of this article.)

of the basalt into the andesite rather than passive underplating and buoyant rise of the mafic magma into the more evolved body, as is common in other systems (Bacon, 1986; Coombs et al., 2003). The enclave basalt is a denser magma and enclaves are less vesicular than the host andesite; enclaves would therefore settle rather than rise. The Stokes settling velocity for the maximum observed enclave size ranges up to 935 m/day. The enclaves must therefore have been incorporated into the andesite magma during eruption in order to remain entrained, with the basaltic magma being injected into the andesite via a pressurized magmatic inlet, because it would not rise passively into the andesite. This is consistent with the eastward propagation of a dike containing the phase 1b magma during the period that Fissure 17 was erupting.

Given this scenario, we must consider the conditions necessary to produce a range of textures from fully homogenized basaltic andesites to basaltic andesite containing minor amounts of enclaves, to relatively unmixed andesites with spatially varying proportions of mafic enclaves along a single fissure. The initial density and viscosity contrast between the phase 1b basalt and the andesite at their respective MgO temperatures (Helz and Thornber, 1987) are sufficient to promote mingling rather than mixing, and the formation of globules rather than interfingering (Semenov and Polyansky, 2017). However, the equilibration temperature of the mingled magmas, as determined by the relative percentages of the two magmas mixing at a given time and location within the magma chamber, likely determines whether the globules will be preserved as enclaves or mingling will proceed further to complete mixing and homogenization. The results of our thermal conduction model suggest that enclave preservation may become possible at a maximum of 38 % basalt but this limit could possibly be as low as 6.4 % basalt as constrained by the maximum volume % of enclaves observed. With these constraints, the largest enclaves would require between 23.5 and 62 h to reach their rheological locking temperature. Phase 1b lavas began erupting at Fissure 16 one day prior to the onset of eruption at Fissure 17, with a three-day break in eruptive activity prior (USGS, 2018). This suggests a timescale for the intrusion of the phase 1b magmas into the andesite magma body prior to eruption of at least one day, but not more than four. This timescale would easily allow enclaves to form and be preserved in the andesitic reservoir during mingling prior to eruption.

The modeled upper threshold in basalt fraction for enclave preservation is generally consistent with the observation that samples from the boomer vent, where enclaves are most prevalent, are estimated to have a basalt contribution to their bulk chemistry of less than 34 %, while the main lava flows and cone where enclaves are rarer range from 31 to 74 % basalt. Peak enclave density along the fissure as shown in Fig. 3 may represent optimum enclave preservation conditions. At the western end of the boomer vent, very little basalt was intruded into the andesite, resulting in few enclaves, and at the far eastern end, too much basalt was intruded for substantial enclave preservation. A visual representation of this scenario is provided in Fig. 11. Given that the boomer vent began and ceased erupting earlier than the main cone, there is also a temporal component to this trend that suggests a general increase in basalt contribution over time.

Our observations of enclave textures, including crenulate margins and overall rounded shapes, as well as mineral exchange between the enclave magma and the host andesite, do not support brittle fragmentation caused by very high strain rates at the basalt-andesite interface, as proposed by Haag et al. (2024). Their evidence supporting the brittle fragmentation hypothesis, fractal distribution of enclave sizes, cannot discriminate between fragmentation/disaggregation in a viscous versus brittle regime using the criteria of Glazner and Mills (2012). Glazner and Mills (2012) emphasize that the departure from fractal distribution seen in the smallest and largest enclaves may be a hallmark of mingling and mixing processes in the ductile regime, but note a fairly broad and overlapping range of possible fractal dimensions for the two processes. Haag et al. (2024) acknowledge the departure of smaller size fractions

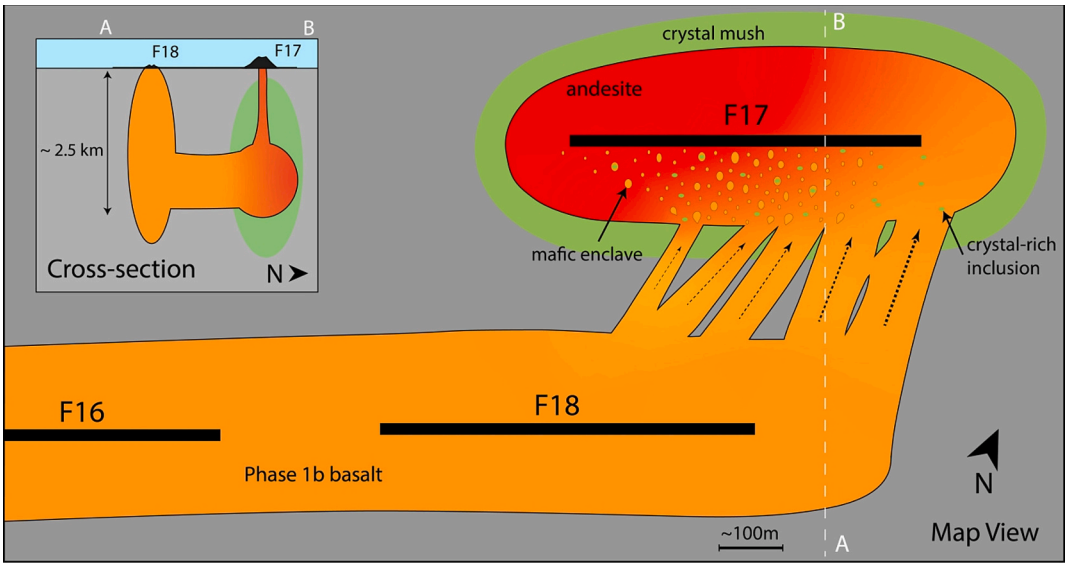

Fig. 11. A simplified schematic representation of Fissure 17 magmatic plumbing showing how different mixing proportions might have allowed formation of enclaves and homogenization of intruding basalt and stored andesite in different proportions along the length of the fissure. The main figure shows a map view while the inset represents a westward-looking cross-section of the magmatic plumbing. This figure represents a scenario in which the crystal-rich inclusions are part of the cumulates of the andesite body.

from fractal distributions in the case of Fissure 17 magmas, but interpret it to result from under-sampling. We propose that conditions of temperature, density and viscosity contrast were appropriate for ordinary mingling, resulting in the formation of globules of the intruding magma that were then preserved by rigidification due to microlite formation. In this case there is no need to invoke unusually high strain rates, either at the point of contact between the basalt and the host andesite or in the conduit during the strombolian eruption of Fissure 17, for which there is no obvious causal mechanism. The rounded, often flattened morphology of the enclaves (Figs. 4, 5 and 6) argues instead for deformation in a ductile regime either at the level of dike injection or during shearing in the conduit. The results of our thermal conduction model as well as the observation of holocrystalline enclaves at other locations in the world (i.e. Chaos Crags, Lassen Volcano, USA (Hootman, 2007); Ilopango Caldera, El Salvador (Richer et al., 2004); Soufriere Hills, Montserrat (Humphreys et al., 2013)), indicate that it is not necessary to invoke a brittle mechanism for the formation of enclaves when substantial quenching does not occur.

The MELTS model (Gualda et al., 2012) used to calculate the temperature-crystallinity relationship for our thermal conduction model predicts that the enclave basalt will still be approximately 41 % liquid by mass on reaching 1060 °C, the temperature of the host andesite. A model run with a maximum enclave radius of 1 cm approaches this scenario with a maximum crystallinity of 58.5 %. This result suggests that holocrystalline enclaves should have crystallized sufficiently to be preserved during intrusion and mingling, and would have been sufficiently brittle to form irregular cracks while in the lava flow, but may have completed their crystallization after eruption.

5. Conclusions

Mafic enclaves found within the andesites and basaltic andesites erupted during the 2018 Lower East Rift Zone eruption of Kīlauea represent the first instance of enclaves detected at Kīlauea. Compositional consistency between the enclaves and the lavas erupted during phase 1b of the eruption, suggest that these magmas likely intruded into an andesite magma body existing in the rift zone to produce a range of basaltic andesites and andesites as well as basaltic enclaves. The early andesites and basalts of 2018 represent a greater compositional contrast than usual at Kīlauea, and this is likely responsible for the formation of enclaves. Field observations, textural and geochemical characterization, and a thermal cooling model suggest that variable mixing proportions of the intruding magma within the andesite magma chamber controlled whether enclaves were preserved, or homogenization occurred in lava erupted at different locations and times along the fissure. The exceptional variability in enclave content along the length of Fissure of 17 provides a unique record of the transition between magma mingling and full hybridization.

CRediT authorship contribution statement

Rose Gallo: Writing – review & editing, Writing – original draft, Software, Methodology, Investigation, Data curation, Conceptualization. **Thomas Shea:** Writing – review & editing, Software, Resources, Methodology, Funding acquisition, Conceptualization. **Alan Whittington:** Writing – review & editing, Supervision, Methodology, Funding acquisition. **Ashley Emerson:** Methodology, Investigation. **Joseph Boro:** Writing – review & editing, Methodology, Investigation, Conceptualization. **Adrien J. Mourey:** Writing – review & editing, Methodology, Investigation.

Declaration of competing interest

The authors declare that they have no known competing financial interests or personal relationships that could have appeared to influence the work reported in this paper.

Data availability

Geochemical data is available in the supplementary tables. Code is available upon request.

Acknowledgments

Funding for this project came from the National Science Foundation grants NSF-EAR 2020045 and NSF EAR Grant 1725321 to TS and NSF-EAR 1928923 to AW. AW and AE were also supported by the UTSA NASA MIRO Center for Advanced Measurements in Extreme Environments (CAMEE), Grant 80NSSC19M019. We thank Wendy Bohrson and an anonymous reviewer for their valuable suggestions for improving the

readability and rigour of this paper. We would like to acknowledge Kelly McCartney, William Nelson, Frank Trusdell, Kendra Lynn and Drew Downs for their assistance in the field, William Nelson and Jason Henry for technical assistance, and A'ja Greene for assistance with sample processing. We would also like to thank the landowners in Leilani Estates and Kapoho who provided us access to their properties for sample collection. TS and JB would like to acknowledge all the local cows for keeping us company at Fissure 17.

Appendix A. Supplementary data

Supplementary data to this article can be found online at https://doi.org/10.1016/j.jvolgeores.2024.108205.

References

Anderson, K.R., Shea, T., Montgomery-Brown, E.K., Swanson, A., Patrick, M.R., Neal, C. A., 2024. The 2018 Eruption of Kılauea: new insights, open questions, and opportunities for volcano science. Annu. Rev. Earth Planet. Sci. 52, 1–40. https://doi.org/10.1146/annurev-earth- 031621-075925.

Andrews, B.J., Manga, M., 2014. Thermal and rheological controls on the formation of mafic enclaves or banded pumice. Contrib. Mineral. Petrol. 167, 961. https://doi.org/10.1007/s00410-013-0961-7.

Annen, C., 2017. Factors affecting the thickness of thermal aureoles. Front. Earth Sci. 5, 82. https://doi.org/10.3389/feart.2017.00082.

Bacon, C.R., 1986. Magmatic inclusions in silicic and intermediate volcanic rocks. J. Geophys. Res. 91, 6091. https://doi.org/10.1029/jb091ib06p06091.

Barbarin, B., Didier, J., 1982. Genesis and evolution of mafic microgranular enclaves through various types of interaction between coexisting felsic and mafic magmas. Geochim. Cosmochim. Acta 46, 115. https://doi.org/10.1016/0016-7037(82)90301-5.

Baxter, S., Feely, M., 2002. Magma mixing and mingling textures in granitoids: examples from the Galway Granite, Connemara, Ireland. Mineral. Petrol. 76, 63–74. https://doi.org/10.1007/s007100200032.

Bottinga, Y., Weill, D., 1970. Densities of liquid silicate systems calculated from partial molar volumes of oxide components. Am. J. Sci. 269, 169–182.

Bresler, L., Shinbrot, T., Metcalfe, G., Ottino, J.M., 1997. Isolated mixing regions: origin, robustness and control. Chem. Eng. Sci. 52, 1623–1636.

Charreteur, G., Tegner, C., 2013. Magmatic emulsion texture formed by mixing during extrusion, Rauðafell composite complex, Breiðdalur volcano, eastern Iceland. Bull. Volcanol. 75, 721. https://doi.org/10.1007/s00445-013-0721-6.

Clynne, M.A., 1999. A complex magma mixing origin for rocks erupted in 1915, Lassen Peak, California. J. Petrol. 40, 105–132.

Coombs, M.L., Eichelberger, J.C., Rutherford, M.J., 2003. Experimental and textural constraints on mafic enclave formation in volcanic rocks. J. Volcanol. Geotherm. 119, 125–144.

Costa, A., Caricchi, L., Bagdassarov, N., 2009. A model for the rheology of particle-bearing suspensions and partially molten rocks: rheology of particle-bearing suspensions. Geochem. Geophys. Geosyst. 10, 13. https://doi.org/10.1029/2008GC002138.

Dietterich, H.R., Diefenbach, A.K., Soule, S.A., Zoeller, M.H., Patrick, M.P., Major, J.J., Lundgren, P.R., 2021. Lava effusion rate evolution and erupted volume during the 2018 Kīlauea lower East Rift Zone eruption. Bull. Volcanol. 83. https://doi.org/10.1007/s00445-021-01443-6.

Downs, D.T., Sas, M., Hazlett, R.W., 2023. Chemistry and petrography of early 19th century basaltic andesites and basalts from the Kamakaiʻa Hills in the Southwest Rift Zone of Kīlauea volcano, Hawaiʻi. J. Volcanol. Geotherm. Res. 444, 107967. https://doi.org/10.1016/j.jvolgeores.2023.107967.

Dragoni, M, 1989. A dynamical model of lava flows cooling by radiation. Bull. Volcanol. 51, 88–95. https://doi.org/10.1007/BF01081978.

Emerson, A., 2023. The Rheological and Thermal History of Kilauea's 2018 Fissure 17 Eruption (M.S). The University of Texas at San Antonio, San Antonio, Texas.

Gansecki, C., Lopaka Lee, R., Shea, T., Lundblad, S.P., Hon, K., Parcheta, C., 2019. The tangled tale of Kīlauea's 2018 eruption as told by geochemical monitoring. Science 366, 1–15. https://doi.org/10.1126/science.aaz0147.

Garcia, M.O., Pietruszka, A.J., Rhodes, J.M., Swanson, K., 2000. Magmatic processes during the prolonged Pu'u 'O'o Eruption of Kilauea volcano, Hawaii. J. Petrol. 41, 967–990. https://doi.org/10.1093/petrology/41.7.967.

Garcia, M.O., Pietruszka, A.J., Rhodes, J.M., 2003. A petrologic perspective of Kilauea volcano's summit magma reservoir. J. Petrol. 44, 2313–2339. https://doi.org/10.1093/petrology/egg079.

Giordano, D., Russell, J.K., Dingwell, D.B., 2008. Viscosity of magmatic liquids: a model. Earth Planet. Sci. Lett. 271, 123–134. https://doi.org/10.1016/j.epsl.2008.03.038.

Glazner, A.F., Mills, R.D., 2012. Interpreting two-dimensional cuts through broken geologic objects: Fractal and non-fractal size distributions. Geosphere 8, 902–914. https://doi.org/10.1130/GES00731.1.

Gualda, G.A.R., Ghiorso, M.S., Lemons, R.V., Carley, T.L., 2012. Rhyolite-MELTS: a modified calibration of MELTS optimized for silica-rich, fluid-bearing magmatic systems. J. Petrol. 53, 875–890. https://doi.org/10.1093/petrology/egr080.

Guo, X., Lange, R.A., Ai, Y., 2014. Density and sound speed measurements on model basalt (An–Di–Hd) liquids at one bar: new constraints on the partial molar volume and compressibility of the FeO component. Earth Planet. Sci. Lett. 388, 283–292. https://doi.org/10.1016/j.epsl.2013.12.005.

Haag, V., Houghton, B.F., Perugini, D., Soldati, A., 2024. Brittle fragmentation of fissure 17 enclave magma revealed by fractal analysis. J. Volcanol. Geotherm. Res. 108087. https://doi.org/10.1016/j.jvolgeores.2024.108087.

Hazlett, R., Orr, T.R., Lundblad, S.P., 2019. Undocumented Late 18th- to Early 19th-Century Volcanic Eruptions in the Southwest Rift Zone of Kīlauea Volcano, Hawaiʻi (no. 5010), Scientific Investigations Report. U.S. Geological Sruvey.

Helz, R.T., Thornber, C.R., 1987. Geothermometry of Kilauea Iki lava lake, Hawaii. Bull. Volcanol. 49, 651–668. https://doi.org/10.1007/BF01080357.

Helz, R.T., Wright, T.L., 1992. Differentiation and magma mixing on Kilauea's east rift zone - a further look at the eruptions of 1955 and 1960. Part I. The late 1955 lavas. Bull. Volcanol. 54, 361–384. https://doi.org/10.1007/BF00312319.

Ho, R.A., Garcia, M.O., 1988. Ho and Garcia 1988 1955 differentiated lavas.Pdf. Bull. Volcanol. 50, 35–46.

Hodge, K.F., Jellinek, A.M., 2012. Linking enclave formation to magma rheology. J. Geophys. Res. B Solid Earth 117. https://doi.org/10.1029/2012JB009393.

Hofmeister, A.M., Sehlke, A., Avard, G., Bollasina, A.J., Robert, G., Whittington, A.G., 2016. Transport properties of glassy and molten lavas as a function of temperature and composition. J. Volcanol. Geotherm. Res. 327, 330–348. https://doi.org/10.1016/j.jvolgeores.2016.08.015.

Hootman, C.D., 2007. Textural Analysis of Mafic Enclaves as an Insight into Magma Mixing Processes at Chaos Crags, Lassen Volcanic Center, California (Master of Science). California State University, Sacramento.

Humphreys, M.C.S., Edmonds, M., Plail, M., Barclay, J., Parkes, D., Christopher, T., 2013. A new method to quantify the real supply of mafic components to a hybrid andesite. Contrib. Mineral. Petrol. 165, 191–215. https://doi.org/10.1007/s00410-012-0805-x.

Kress, V.C., Carmichael, I.S.E., 1991. The compressibility of silicate liquids containing Fe203 and the effect of composition, temperature, oxygen fugacity and pressure on their redox states. Contrib. Mineral. Petrol. 108, 82–92.

Lange, R.A., Carmichael, I.S.E., 1987. Densities of Na20-K20-Ca0-Mg0-Fe0-Fe203-A1203-Ti02-Si02 liquids: New measurements and derived partial molar properties. Geochim. Coemochim. Acta 51, 293I–2946.

Lejeune, A., Richet, P., 1995. Rheology of crystal-bearing silicate melts: an experimental study at high viscosities. J. Geophys. Res. 100, 4215–4229. https://doi.org/10.1029/94JB02985.

Lerner, A.H., Wallace, P.J., Shea, T., Mourey, A.J., Kelly, P.J., Nadeau, P.A., Elias, T., Kern, C., Clor, L.E., Gansecki, C., Lee, R.L., Moore, L.R., Werner, C.A., 2021. The Petrologic and Degassing Behavior of Sulfur and Other Magmatic Volatiles from the 2018 Eruption of Kīlauea, Hawaiʻi: Melt Concentrations, Magma Storage Depths, and Magma Recycling, Bulletin of Volcanology. Springer, Berlin Heidelberg. https://doi.org/10.1007/s00445-021-01459-y.

Liu, Q., Lange, R.A., 2006. The partial molar volume of Fe2O3 in alkali silicate melts: evidence for an average Fe3+ coordination number near five. Am. Mineral. 91, 385–393. https://doi.org/10.2138/am.2006.1902.

Liu, E.J., Cashman, K.V., Rust, A.C., 2015. Optimising shape analysis to quantify volcanic ash morphology. GeoResJ 8, 14–30. https://doi.org/10.1016/j.grj.2015.09.001.

Lubbers, J., Kent, A., Russo, C., 2023. LaserTRAM-DB: A Time Resolved Analysis Module for the Complete Reduction of Laser Ablation Inductively Coupled Plasma Mass Spectrometry Data. Doi:10.31223/X5QG95.

Mader, H.M., Llewellin, E.W., Mueller, S.P., 2013. The rheology of two-phase magmas: a review and analysis. J. Volcanol. Geotherm. Res. 257, 135–158. https://doi.org/10.1016/j.jvolgeores.2013.02.014.

Mancini, A., Mattsson, H.B., Bachmann, O., 2015. Origin of the compositional diversity in the basalt-to-dacite series erupted along the Heiðarsporður ridge, NE Iceland. J. Volcanol. Geotherm. Res. 301, 116–127. https://doi.org/10.1016/j.jvolgeores.2015.05.010.

Martin, V.M., Holness, M.B., Pyle, D.M., 2006a. Textural analysis of magmatic enclaves from the Kameni Islands, Santorini, Greece. J. Volcanol. Geotherm. Res. 154, 89–102. https://doi.org/10.1016/j.jvolgeores.2005.09.021.

Martin, V.M., Pyle, D.M., Holness, M.B., 2006b. The role of crystal frameworks in the preservation of enclaves during magma mixing. Earth Planet. Sci. Lett. 248, 787–799. https://doi.org/10.1016/j.epsl.2006.06.030.

Mashima, H., 2004. Time scale of magma mixing between basalt and dacite estimated for the Saga-Futagoyama volcanic rocks in Northwest Kyushu, Southwest Japan. J. Volcanol. Geotherm. Res. 131, 333–349. https://doi.org/10.1016/S0377-0273(03)00412-8.

Moore, R.B., Trusdell, F.A., 1991. Geologic Map of the Lower East Rift Zone of Kilauea Volcano, Hawaii. U.S. Geological Survey Miscellaneous Investigations Map I, p. 2225.

Mourey, A.J., Shea, T., Lynn, K.J., Lerner, A.H., Lambart, S., Costa, F., Oalmann, J., Lee, R.L., Gansecki, C., 2022. Trace elements in olivine fingerprint the source of 2018 magmas and shed light on explosive-effusive eruption cycles at Kīlauea Volcano. Earth Planet. Sci. Lett. 595, 117769. https://doi.org/10.1016/j.epsl.2022.117769.

Mourey, A.J., Shea, T., Costa, F., Shiro, B., Longman, R.J., 2023. Years of magma intrusion primed Kīlauea Volcano (Hawai'i) for the 2018 eruption: evidence from olivine diffusion chronometry and monitoring data. Bull. Volcanol. 85, 18. https://doi.org/10.1007/s00445-023-01633-4.

Namiki, A., Tanaka, Y., 2017. Oscillatory rheology measurements of particle and bubble-bearing fluids: solid-like behavior of a crystal-rich basaltic magma. Geophys. Res. Lett. 44, 8804–8813. https://doi.org/10.1002/2017GL074845.

Neal, C.A., Brantley, S.R., Antolik, L., Babb, J.L., 2019. The 2018 rift eruption and summit collapse of Kīlauea Volcano. Science 363, 367–374.

Ochs, F.A., Lange, R.A., 1999. The density of hydrous magmatic liquids. Science 283, 1314–1317. https://doi.org/10.1126/science.283.5406.1314.
Patrick, M.R., Dietterich, H.R., Lyons, J.J., Diefenbach, A.K., Parcheta, C., Anderson, K. R., Namiki, A., Sumita, I., Shiro, B., Kauahikaua, J.P., 2019. Cyclic lava effusion during the 2018 eruption of Kīlauea Volcano. Science 366. https://doi.org/10.1126/science.aay9070.
Petrelli, M., Perugini, D., Poli, G., 2006. Time-scales of hybridisation of magmatic enclaves in regular and chaotic flow fields: petrologic and volcanologic implications. Bull. Volcanol. 68, 285–293. https://doi.org/10.1007/s00445-005-0007-8.
Petrelli, M., Perugini, D., Poli, G., 2011. Transition to chaos and implications for time-scales of magma hybridization during mixing processes in magma chambers. Lithos 125, 211–220. https://doi.org/10.1016/j.lithos.2011.02.007.
Pietruszka, A.J., Garcia, M.O., 1999. The size and shape of Kilauea Volcano's summit magma storage reservoir: a geochemical probe. Earth Planet. Sci. Lett. 167, 311–320. https://doi.org/10.1016/S0012-821X(99)00036-9.
Pietruszka, A.J., Garcia, M.O., Rhodes, J.M., 2021. Accumulated Puʻu ʻŌʻō magma fed the voluminous 2018 rift eruption of Kīlauea Volcano: evidence from lava chemistry. Bull. Volcanol. 83. https://doi.org/10.1007/s00445-021-01470-3.
Plail, M., Edmonds, M., Woods, A.W., Barclay, J., Humphreys, M.C.S., Herd, R.A., Christopher, T., 2018. Mafic enclaves record syn-eruptive basalt intrusion and mixing. Earth Planet. Sci. Lett. 484, 30–40. https://doi.org/10.1016/j.epsl.2017.11.033.
Richer, M., Mann, C.P., Stix, J., 2004. Mafic magma injection triggers eruption at Ilopango Caldera. In: Natural Hazards in El Salvador. Geological Society of America Special Paper. Geological Society of America, Boulder, Colorado, pp. 175–189.
Ruprecht, P., Simon, A.C., Fiege, A., 2020. The survival of mafic magmatic enclaves and the timing of magma recharge. Geophys. Res. Lett. 47. https://doi.org/10.1029/2020GL087186.
Schneider, C.A., Rasband, W.S., Eliceiri, K.W., 2012. NIH image to ImageJ: 25 years of image analysis. Nat. Methods 9, 671–675. https://doi.org/10.1038/nmeth.2089.
Seaman, S.J., Chapman, M., 2008. The fate of basaltic enclaves during pyroclastic eruptions: an origin of andesitic ignimbrites. J. Volcanol. Geotherm. Res. 178, 671–682. https://doi.org/10.1016/j.jvolgeores.2008.07.027.
Semenov, A.N., Polyansky, O.P., 2017. Numerical modeling of the mechanisms of magma mingling and mixing: a case study of the formation of complex intrusions. Russ. Geol. Geophys. 58, 1317–1332. https://doi.org/10.1016/j.rgg.2017.11.001.
Shamberger, P.J., Garcia, M.O., 2007. Geochemical modeling of magma mixing and magma reservoir volumes during early episodes of Kīlauea Volcano's Puʻu ʻŌʻō eruption. Bull. Volcanol. 69, 345–352. https://doi.org/10.1007/s00445-006-0074-5.
Soldati, A., Houghton, B.F., Dingwell, D.B., 2021. Subliquidus rheology of basalt from the 2018 lower East Rift Zone Kilauea eruption: isothermal vs. dynamic expression. Chem. Geol. 581, 120363. https://doi.org/10.1016/j.chemgeo.2021.120363.
Soldati, A., Weidendorfer, D., Cimarelli, C., Kueppers, U., Houghton, B.F., Tisdale, C.M., Dingwell, D.B., 2024. Crystal mush interaction controls eruptive style during the 2018 Kīlauea fissure eruption. J. Volcanol. Geotherm. Res. 454, 108178. https://doi.org/10.1016/j.jvolgeores.2024.108178.
Sparks, R.S.J., Marshall, L.A., 1986. Thermal and mechanical constraints on mixing and mafic and silicic magmas. J. Volcanol. Geotherm. Res. 29, 99–124.
USGS, 2018. Kīlauea Volcano – 2018 Summit and Lower East Rift Zone (LERZ) Brief Overview of Events April 17 to July 22.
Vernon, R.H., 1984. Microgranitoid enclaves in granitesglobules of hybrid magma quenched in a plutonic environment. Lett. Nat. 309, 438–439. https://doi.org/10.1038/309438a0.
Wieser, P.E., Edmonds, M., Gansecki, C., Maclennan, J., Jenner, F.E., Kunz, B., Antoshechkina, P., Trusdell, F., Lee, R.L., EIMF, 2022. Explosive activity on Kīlauea's lower East Rift Zone Fueled by a Volatile-Rich, Dacitic Melt. Geochem. Geophys. Geosyst. 23. https://doi.org/10.1029/2021gc010046.
Winslow, H., Ruprecht, P., Gonnermann, H.M., Phelps, P.R., Muñoz-Saez, C., Delgado, F., Pritchard, M., Amigo, A., 2022. Insights for crystal mush storage utilizing mafic enclaves from the 2011–12 Cordón Caulle eruption. Sci. Rep. 12, 9734. https://doi.org/10.1038/s41598-022-13305-y.
Wolff, J.A., 2021. Felsic igneous rocks. In: Encyclopedia of Geology. Elsevier, pp. 145–169. https://doi.org/10.1016/B978-0-12-409548-9.12539-4.
Wright, T.L., 1971. Chemistry of Kilauea and Mauna Loa Lava in Space and Time, (Geological Survey Professional Paper No. 735). U.S. Geological Survey, Washington.
Wright, T.L., Fiske, R.S., 1971. Origin of the differentiated and hybrid lavas of Kilauea Volcano, Hawaii. J. Petrol. 12, 1–65. https://doi.org/10.1093/petrology/12.1.1.
Wright, T.L., Helz, R.T., 1996. Differentiation and magma mixing on Kilauea's east rift zone: a further look at the eruptions of 1955 and 1960. Part II. The 1960 lavas. Bull. Volcanol. 57, 602–630.